CrossMark

Influence of hydrological, biogeochemical and temperature transients on subsurface carbon fluxes in a flood plain environment

Bhavna Arora · Nicolas F. Spycher · Carl I. Steefel · Sergi Molins ·
Markus Bill · Mark E. Conrad · Wenming Dong · Boris Faybishenko ·
Tetsu K. Tokunaga · Jiamin Wan · Kenneth H. Williams · Steven B. Yabusaki

Abstract Flood plains play a potentially important role in the global carbon cycle. The accumulation of organic matter in flood plains often induces the formation of chemically reduced groundwater and sediments along riverbanks. In this study, our objective is to evaluate the cumulative impact of such reduced zones, water table fluctuations, and temperature gradients on subsurface carbon fluxes in a flood plain at Rifle, Colorado located along the Colorado River. 2-D coupled variably-saturated, non-isothermal flow and biogeochemical reactive transport modeling was applied to improve our understanding of the abiotic and microbially mediated reactions controlling carbon dynamics at the Rifle site. Model simulations considering only abiotic reactions (thus ignoring microbial reactions) underestimated CO_2 partial pressures observed in the unsaturated zone and severely underestimated inorganic (and overestimated organic)

carbon fluxes to the river compared to simulations with biotic pathways. Both model simulations and field observations highlighted the need to include microbial contributions from chemolithoautotrophic processes (e.g., Fe^{+2} and S^{-2} oxidation) to match locally-observed high CO_2 concentrations above reduced zones. Observed seasonal variations in CO_2 concentrations in the unsaturated zone could not be reproduced without incorporating temperature gradients in the simulations. Incorporating temperature fluctuations resulted in an increase in the annual groundwater carbon fluxes to the river by 170 % to 3.3 g m^{-2} d^{-1}, while including water table variations resulted in an overall decrease in the simulated fluxes. We conclude that spatial microbial and redox zonation as well as temporal fluctuations of temperature and water table depth contribute significantly to subsurface carbon fluxes in flood plains and need to be represented appropriately in model simulations.

B. Arora (✉) · N. F. Spycher · C. I. Steefel ·
S. Molins · M. Bill · M. E. Conrad · W. Dong ·
B. Faybishenko · T. K. Tokunaga · J. Wan ·
K. H. Williams
Energy Geosciences Division, Lawrence Berkeley
National Laboratory, 1 Cyclotron Rd., MS 74-327R,
Berkeley, CA 94720, USA
e-mail: barora@lbl.gov

S. B. Yabusaki
Pacific Northwest National Laboratory, Richland, USA

Introduction

The quantification of carbon fluxes in soils and groundwater is critical for closing key biogeochemical cycles and for developing a predictive understanding

Springer

of climate change scenarios. Soil CO_2 dynamics are difficult to predict because of the presence of several carbon sources and sinks, as well as different hydrological and biogeochemical mechanisms that affect its uptake and release (Suchomel et al. 1990; Hope et al. 1994; Hanson et al. 2000; Andrews et al. 2011). CO_2 fluxes in near-surface environments are primarily affected by atmospheric exchange, root zone biogeochemical processes, and microbial respiration (e.g., Wood and Petraitis 1984; Schlesinger and Andrews 2000; Crow and Wieder 2005). The origin of CO_2 at depth has been attributed to aerobic and anaerobic degradation of dissolved organic carbon, inorganic processes involving carbonate minerals, and the effects of vertical temperature gradients and water table fluctuations (Keller and Bacon 1998; Etiope 1999; Walvoord et al. 2005; Fan et al. 2014). Among these processes, the rates of organic matter degradation and production of CO_2 are strongly dependent on microbial community structure and function (Waldrop et al. 2000; Schmidt et al. 2011; Southwell and Thoms 2011; Steefel et al. 2014). Abiotic reactions, such as precipitation and dissolution of calcite, have a significant effect on pH and solution chemistry (Stumm and Morgan 1993; Macpherson 2009). Given the complex and coupled nature of hydrological and biogeochemical processes controlling CO_2 fluxes in the subsurface, soil carbon budgeting can benefit from reactive transport simulations that can be used to identify the contributions of the different processes within both unsaturated and saturated zones (e.g., Simunek and Suarez 1993; Thornton and McManus 1994; Doussan et al. 1997; Druhan et al. 2014b)

Although atmospheric CO_2 exchanges are thought to be several times greater than subsurface exports (Pulliam 1992; Richey et al. 2002), groundwater exports from terrestrial sources and flood plain environments to aquatic ecosystems also constitute an important part of the global carbon cycle. Several studies have debated the role of rivers as passive or active transporters of carbon to the ocean (Cole and Caraco 2001; Richey et al. 2002; Cole et al. 2007; Aufdenkampe et al. 2011). In either case, inorganic and organic carbon exports exert an important control on aquatic respiration, carbonate buffering and pH control, as well as CO_2 degassing in rivers and other aquatic environments (Brunke and Gonser 1997; Aufdenkampe et al. 2011). However, significant uncertainty is associated with the prediction of these subsurface exports, particularly due to the influence of climatic variations, land-use changes, and human disturbances. The spatiotemporal variability of subsurface carbon fluxes thus needs to be better understood.

Temporal variability in carbon concentrations has been linked to rainfall events, seasonality of flow, evapotranspiration, and temperature fluctuations (e.g., Hinton et al. 1997; Arora et al. 2013; Kang et al. 2014). For example, Leirós et al. (1999) stressed the importance of seasonal variability on soil carbon and nitrogen mineralization rates. Changes in microbial community structure and activity have also been correlated with seasonal and annual temperature and precipitation variability and with the fate of carbon (Parton et al. 1987; Zogg et al. 1997; Waldrop et al. 2000; Wilhelm et al. 2014). There are thus several drivers of temporal variability in carbon fluxes, such as hydrological processes and climatic variables (Kalbitz et al. 2000; Dai et al. 2012; Atkins et al. 2013; Jansen et al. 2014). However, many studies have argued that temperature and soil moisture are two primary controls on CO_2 production rates (Raich and Potter 1995; Smith et al. 2003; Stielstra et al. 2015). In particular, several studies have conducted soil warming experiments to suggest that changes in microbial biomass and resulting soil CO_2 fluxes are due to these controls (Eliasson et al. 2005; Dermody et al. 2007; Frey et al. 2008).

Spatial variability in carbon concentrations has been linked to landscape patterns, hydrological connectivity, and heterogeneous subsurface properties (e.g., Dick et al. 2014; Southwell and Thoms 2011; Tockner et al. 1999). For example, Andrews et al. (2011) suggested that swales had higher solid and dissolved organic carbon content across the Shale Hills Catchment, Pennsylvania due to their landscape position and hydrological connectivity. Similarly, reduced zones in alluvial aquifers adjacent to rivers are known to exert a strong control on the transformation and redox dynamics of carbon and nutrients in flood plain environments due to their distinct biogeochemical properties (e.g., Bourg and Bertin 1993). In this context, emphasis has been given to the role of reduced zones in river bank filtration (e.g., Doussan et al. 1997; Hiscock and Grischek 2002; Tufenkji et al. 2002) and metal assimilation (e.g., Gandy et al. 2007; Lynch et al. 2014). Albeit involving similar biogeochemical concepts, the present study focuses instead

Fig. 1 Rifle site map with the location of the modeled "TT" transect and the spatial distribution of naturally reduced zones (NRZ). The mapping of NRZs using a combination of induced polarization methods and Bayesian techniques is presented in more detail by Wainwright et al. (2015)

– – Groundwater flow direction —— Modeled transect ■ Naturally reduced sediments
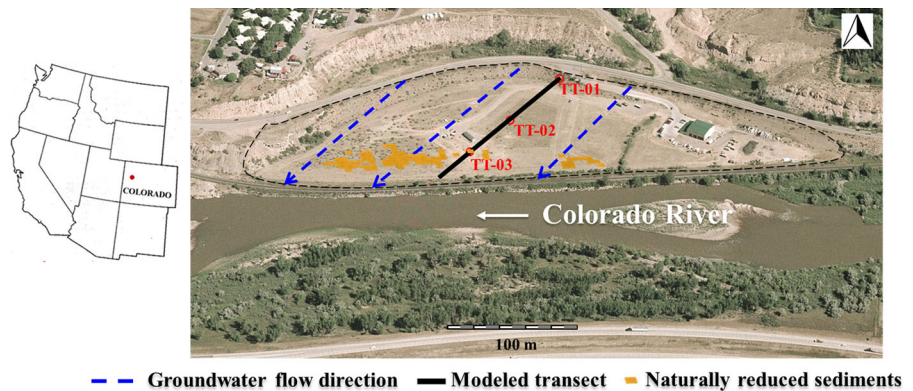
on the persistence and impact of reduced zones on subsurface carbon exports during conditions of aquifer discharge to a river.

Here we focus on the U.S. Department of Energy (DOE) site at Rifle, Colorado (USA) (Fig. 1), where reduced zones have been observed within the alluvial aquifer beneath the Rifle flood plain (described in more detail below) and are associated with the accumulation of Fe(II) and non-volatile sulfides in sediments close to the stream banks of the Colorado River (Lovley and Phillips 1986; Bargar et al. 2011; Lynch et al. 2014). Such areas are commonly referred to as "naturally reduced zones" (NRZs) within the Rifle site community to distinguish them from areas where reducing conditions have developed from bio-stimulation experiments. These NRZ's have the ability to scavenge metals and oxidants due to their typically elevated levels of sediment-associated organic matter as compared to non-reduced flood plain sediments (Campbell et al. 2012; Qafoku et al. 2014). Because these NRZs occur primarily down-gradient of the site (roughly paralleling the Colorado River) (Wainwright et al. 2015), the study of their spatial distribution presents a unique opportunity to test conceptual models of redox dynamics at the field-scale using reactive transport simulations.

In this study, we test a conceptual model where the spatial organization of a naturally reduced zone is dependent on the interactions between oxygenated groundwater and initially homogeneous (reduced) flood plain sediments. Although the NRZs have been studied at the Rifle site in the context of understanding their geochemical characteristics and/or uranium sequestration abilities, to our knowledge, this is the first study in which a numerical model is applied to simulate the persistence of these NRZs in the presence

of a constant up-gradient oxic recharge, beginning initially from uniformly reducing conditions throughout the modeled domain. Furthermore, these simulations provide a foundation for detailed assessment of the relative contributions of abiotic and biotic processes as well as the primary factors (soil moisture, temperature) controlling the spatiotemporal variability of carbon fluxes from the site to the atmosphere and the Colorado River.

The objectives of this study are to develop and apply the conceptual modeling framework to: (1) quantify the release of carbon dioxide via abiotic processes, heterotrophic pathways, and autotrophic microbial oxidation of both reduced aqueous species (e.g., Fe^{+2}, HS^-) and minerals (e.g., pyrite), and (2) investigate the effects of reduced zones as well as water table variations and temperature gradients on subsurface carbon dynamics at the Rifle site. To reach these objectives, a biogeochemical reaction network (Fig. 2) was built based on knowledge from previous modeling and experimental efforts at the site. The current modeling study targets a portion of the Rifle field site unaffected by previous groundwater remedial activities (e.g., Williams et al. 2011), incorporates new information on chemolithoautotrophs using a reduced-order geochemical reaction network, and tests the spatial extent of naturally reduced zones adjacent to the river under continued influx of oxygenated groundwater.

Study site

Comprehensive descriptions of the Rifle site have been presented elsewhere (U.S. Department of Energy 1999; Anderson et al. 2003; Vrionis et al. 2005;

Fig. 2 Schematic representation of the biogeochemical reaction network included in model simulations. Some microbially-mediated pathways are explicitly represented in the reaction network (such as Sulfuricurvum as sulfide oxidizer) while the broader diversity of species for other functions (such as sulfate reducers) is captured by simplified, overall reactions and rates (Table 5)
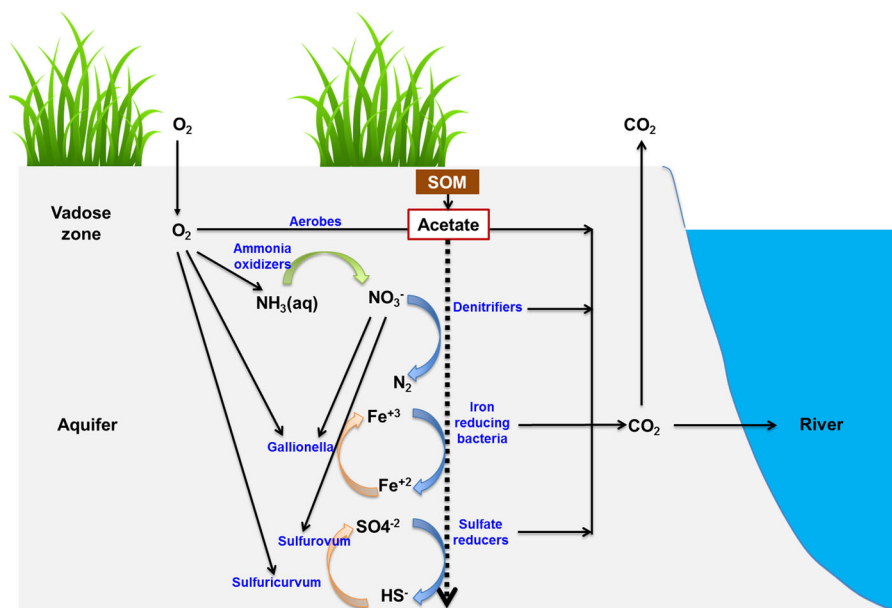
Williams et al. 2011) and thus the environmental conditions of the site are only briefly summarized here. The Rifle site is a former uranium and vanadium ore processing facility in western Colorado that operated from 1924 through 1958 (U.S. Department of Energy 1999). Subsequently, the mill tailings and impacted alluvial sediments were removed and the site was capped with a locally-derived fill material, and then revegetated. In spite of these near-surface cleanup efforts, groundwater at the site has remained contaminated with uranium at the micromolar level (Fang et al. 2009; Li et al. 2010; Fox et al. 2012).

Groundwater at the site flows through alluvial flood plain deposits, which are mainly comprised of unconsolidated gravel and cobbles, but are also interspersed with fine grained silt and clay and locally organic-rich sediments (U.S. Department of Energy 1999; Campbell et al. 2012; Tokunaga et al. 2015). The alluvial deposits are 6–7 m thick and include approximately 2 m of the fill material underlain by the relatively impermeable Wasatch formation (Figs. 1, 3). The depth to groundwater averages between 3 and 4 m depending on the Colorado River stage (Fang et al. 2009; Yabusaki et al. 2011). The variability in groundwater flow and direction is short-lived and has been linked to Colorado River stage fluctuations as well as seasonal precipitation, which averages approximately 300 mm annually (Arora et al. 2015a).

Groundwater flows generally southwest to the river because of significant aquifer recharge by rainfall, snow melt, and irrigation ditches up-gradient of the site (U.S. Department of Energy 1999). The hydraulic conductivity (0.06–20 m day^{-1}) and pore water velocity (0.1–0.6 m day^{-1}) vary across the site depending upon the local lithology (Williams et al. 2011; Yabusaki et al. 2011). Minerals reported in the sediments include quartz and calcite with lesser amount of clays and iron-bearing minerals, such as goethite, magnetite, and hematite (Campbell et al. 2012). Both the physical properties and geochemical characteristics of these sediments, including the abundance of the Fe-oxyhydroxides vary spatially across the site. Whereas NRZ sediments are associated with elevated concentrations of natural organic matter and reduced mineral phases such as framboidal pyrite, the abundance of these phases is much lower outside the NRZ sediments (Qafoku et al. 2009; Kukkadapu et al. 2010; Qafoku et al. 2014).

The biogeochemical interactions of uranium, iron, sulfate and carbon species in NRZ sediments at the site are markedly different from those observed in background aquifer sediments (Flores Orozco et al. 2011; Campbell et al. 2012; Bao et al. 2014; Qafoku et al. 2014). The dissolved oxygen uptake rates in these two contrasting zones also differ significantly (Long 2009; U.S. Department of Energy 2012). Arora et al. (2015a)

Fig. 3 2-D cross section of the model domain (modified from Tokunaga et al. (2015))
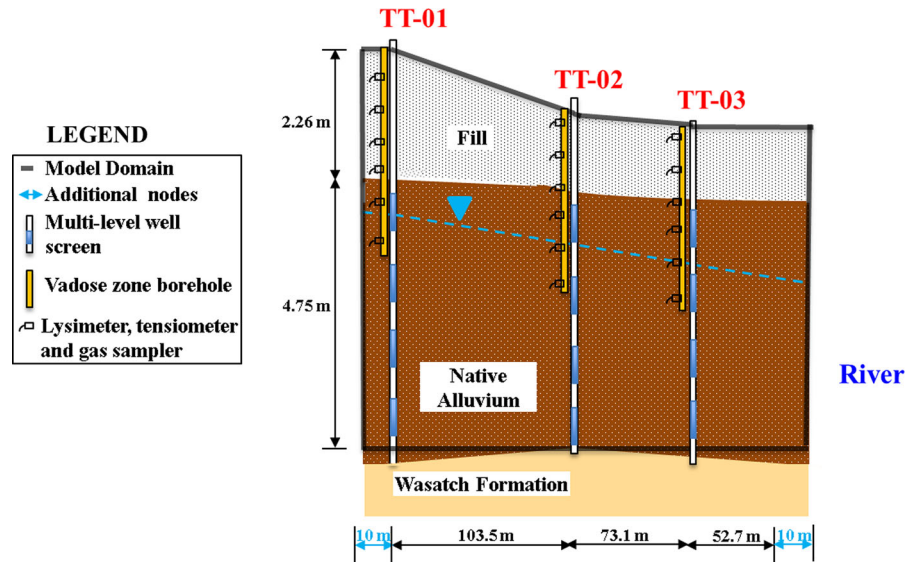
reported that geochemical hot moments (McClain et al. 2003) associated with both conservative and reactive species in the NRZ's occur at different dominant frequencies than those found in other zones at the site. Because of this spatial variability and complexity, we model a well-instrumented transect of the Rifle site (two-dimensional x–z model domain) that is approximately parallel to the general groundwater flow direction and which includes both the saturated and unsaturated zones as well as a naturally reduced (NRZ) location.

The transect (referred to as the "TT" transect) includes three wells, TT-01, TT-02, and TT-03 installed in 2013 (Figs. 1, 3). Well TT-01 is located furthest north, hydrologically up-gradient from the river, TT-02 is within the central flood plain, and TT-03 is a down-gradient well situated within a previously characterized NRZ within ca. 50 m of the Colorado River (Campbell et al. 2012). A detailed description of the TT transect and the well instrumentation was given by Tokunaga et al. (2015) and Williams et al. (2011). Our model relies in large part on hydrologic and geochemical data from these authors. Tokunaga et al. (2015) and Williams et al. (2011) installed separate boreholes to sample the unsaturated and saturated zones. For vadose zone sampling, instrumentation sets were installed at various depths up to 3.5 m and included tensiometers, thermistors (at TT-03 only), and soil water and gas samplers. For CO_2 analysis, pore gas from all ports above the water table samples were

collected using a peristaltic pump and injected into evacuated serum vials capped with blue butyl rubber septa. CO_2 concentrations were quantified on a GC-2014 Shimadzu gas chromatograph. Using a gas tight syringe, 4.5 mL of sample aliquot was injected into a 1 mL stainless steel loop mounted on a 10-port valve (Valco). CO_2 was separated on a packed HayeSep-D column (4 m × 1/8 inch). CO_2 was reduced to CH_4 in a methanizer. Reduced CO_2 was quantified using a flame ionization detector (FID). Groundwater sampling was carried out at three discrete levels—an upper zone in the capillary fringe which becomes saturated during the annual peak height of the water table, a zone about 1 m below the typical minimum water table depth, and the deepest portion of the aquifer. In particular, bicarbonate was measured as TIC (total inorganic carbon) directly from the pore water samples using a Shimadzu TOC-V$_{CPH}$ analyzer.

Model development

Our biogeochemical model for carbon fate and transport was built in a domain of the Rifle site that is generally representative of a flood plain environment. A conceptual model is adopted in which the lateral extent of the reduced zone adjacent to the river is controlled by the influx of oxygenated groundwater up-gradient from the river bank along the lateral flood plain accretion boundary, as described further below.

Conceptual model

The Rifle flood plain site is situated where a former river channel left behind a crescent-shaped meander scar and several meters of flood plain alluvium (U.S. Department of Energy 1999) (Fig. 1). Flood plain sediments originating from overbank deposition, channel deposition, or flood events are widely known to accumulate organic matter that include surficial plants and woody debris (Miall 2001; Blazejewski et al. 2009; Wójcicki 2012). Although the composition and abundance of organic matter may vary from one depositional environment to another, the accumulation and degradation of organic matter is known to create reducing conditions adjacent to rivers (e.g., Bourg and Bertin 1993) and accumulation of trace metals (e.g., van Griethuysen et al. 2005; Wójcicki and Marynowski 2012; Helz and Adelson 2013). Similarly, naturally reduced sediments along the river at the Rifle site are enriched with organic matter, U, and reduced Fe and S phases. Campbell et al. (2012) compared these reduced zones to roll-type uranium ore deposits, where sharp redox fronts develop when oxidizing recharge groundwater meets reducing conditions induced by organic matter degradation (e.g., Harshman 1972; Spirakis 1996). The lateral extent of the NRZs along the stream banks of the Colorado River are likely controlled by similar processes, including the rate of oxidation by groundwater recharge up-gradient of the shore and the deposition of organic matter. Note that no correlation was found between spatial distribution of NRZs and clay content or lower permeability zones at the Rifle site (Wainwright et al. 2015). Following this conceptual model, we simulate the persistence and lateral extent of an NRZ next to the river margin starting with uniformly distributed organic matter and reducing conditions across the modeled transect, then simulating the recharge of more oxidizing groundwater up-gradient of the transect (as well as minor precipitation above it) towards the river. Thus, in our model the NRZ develops over time from an initially homogeneous distribution of carbon and reduced phases. We test this conceptual model as a generic representation of redox-transitional zones which can be easily transferred to other flood plain environments.

Modeling approach

To represent the geochemical system, the reactive transport code TOUGHREACT V3-OMP (Xu et al. 2011; Sonnenthal et al. 2014) was used. Several reactive transport simulations were run in which the degradation and oxidation of organic matter was simulated with increasing levels of complexity (Table 1; Fig. 2). The simulations were divided into two categories—the first set of simulations (S1, S2 and S3) focused on steady water table and temperature conditions. One goal with these simulations was to

Table 1 Reactive transport simulations considered in this study

Simulation	Description	Reactions considered	Water level	Temperature
Steady water table and fixed temperature simulations				
S1	Base case simulation (no microbial reactions)	Table 4	Constant levels	Constant T (12 °C)
S2	S1 + microbial contributions from heterotrophic processes	S1 + Table 5 (R_{O_2}, $R_{NO_3^-}$, $R_{NO_2^-}$, R_{NH_3}, and $R_{SO_4^{-2}}$)	Constant levels	Constant T (12 °C)
S3	S1 + microbial contributions from heterotrophic and chemolithoautotrophic processes	S2 + Table 5 ($R_{O_2-HS^-}$, $R_{O_2-Fe^{+2}}$, $R_{NO_3^--HS^-}$ and $R_{NO_3^--Fe^{+2}}$)	Constant levels	Constant T (12 °C)
Simulations to capture short-term water table rise and temperature gradients				
S3.1	S3 + water table rise in the April–June 2013 time frame	Same as S3	Fluctuating	Constant T (12 °C)
S3.1′	S3 + water table fluctuations in the April 2013–April 2014 time frame	Same as S3	Fluctuating	Constant T (12 °C)
S3.2	S3 + temperature gradient on June 2013	Same as S3	Constant levels	Fixed gradient
S3.2′	S3 + temperature fluctuations in the April 2013–April 2014 time frame	Same as S3	Constant levels	Fluctuating

obtain nearly steady chemical conditions that are generally representative of the field data (average pH, aqueous and gaseous concentrations, etc.) and result in the persistence of the NRZ near the TT-03 well location. The second set of simulations (S3.1 and S3.2) was restarted from the selected base case simulation (S3) to evaluate CO_2 fluxes under seasonal water table variations (S3.1) and temperature gradients (S3.2). An estimate of carbon exports from the Rifle site to the Colorado River under steady (S1, S2, S3) and transient conditions (S3.1', S3.2') is also reported. Simulations S3.2 and S3.2' were run in a manner so as to clearly distinguish temperature effects from abiotic and biotic processes. A detailed description of the different simulations is provided in Biotic reactions with chemolithoautotrophic pathways (S3) section.

Numerical model

TOUGHREACT was used together with the EOS9 equation of state module (Pruess et al. 1999) for isothermal simulations. The EOS9 module implements Richards' equation (Richards 1931) for variably saturated flow of a single aqueous phase with air treated as a passive phase under conditions of constant pressure and temperature. Simulations considering variable temperature were run using the EOS3 module (Pruess et al. 1999), which simulates non-isothermal, multiphase (water, air) flow processes in variably saturated porous media. The model discretization, inputs and boundary conditions are summarized below.

Model domain and discretization

The modeling domain consists of a two-dimensional (x–z) cross-section about 230 m long (along the regional direction of groundwater flow) and 7 m deep (Fig. 3). The domain was discretized using a total of 8050 grid blocks with a uniform grid spacing of 1 m along the horizontal direction and 0.2 m along the vertical direction. The fill and alluvium stratigraphic units were represented, and the top of the underlying, much less permeable, Wasatch Formation was chosen as the lower boundary of the domain. Homogeneous geochemical and hydrogeological properties were initially assumed within each unit (as described in the next section). A maximum time step of 1 day was used for all simulations.

Hydrological, thermal and transport properties

The average hydrological properties of the fill and alluvium were estimated using pedotransfer functions from textural data of sediments from the site. These values are summarized in Table 2.

An aqueous phase diffusion coefficient of $1.5 \times 10^{-9} \ m^2 \ s^{-1}$ was used for all aqueous species in all the simulations. The diffusion coefficient of gaseous CO_2 was dynamically computed as a function of temperature and molecular diameter (Lasaga 1998, Eq. 322), yielding values ranging from 1.74×10^{-5} to $1.87 \times 10^{-5} \ m^2 \ s^{-1}$ between 10 and 24 °C. In all simulations, these diffusion coefficients are multiplied by a tortuosity factor (ranging between 0 and 1) to yield effective diffusion coefficients, and the tortuosity factor is dynamically (and locally) computed as a function of liquid saturation and porosity following the Millington-Quirk model (Millington and Quirk 1961). Tortuosity factors computed in this way are quite sensitive to liquid saturation and lower the gas diffusivity by about 1, 2, and 3 orders of magnitude at liquid saturations of 0.4, 0.7, and 0.85 respectively (Fig. A1, Appendix 1). Relevant thermal properties used in the simulations are listed in Table 3.

Geochemical system

The key geochemical processes included in this study are aqueous speciation, mineral precipitation/dissolution reactions, and microbially mediated redox reactions. The primary species in the modeled reaction network include H^+, HCO_3^-, Al^{+3}, Ca^{+2}, Cl^-, Fe^{+3}, Fe^{+2}, K^+, Mg^{+2}, $NH_3(aq)$, NO_3^-, NO_2^-, Na^+, $N_2(aq)$, $O_2(aq)$, HS^-, SO_4^{-2}, $SiO_2(aq)$, and acetate. The aqueous speciation reactions and their equilibrium constants are listed in Table 10 in the Appendix.

The mineralogy of the aquifer sediments was assigned on the basis of previous studies at the site (Li et al. 2009; Fang et al. 2009; Campbell et al. 2012; Qafoku et al. 2014). Based on these studies, calcite, siderite, goethite and pyrite were included in the reaction network. The precipitation and dissolution of these minerals were modeled using kinetic rate laws (Table 4). The equilibrium constants for mineral precipitation/dissolution reactions are listed in Table 11 in the Appendix.

Although the biodegradation of organic carbon is usually simulated through several reactive fractions

Table 2 Physical model parameters used in the simulations

Hydrostratigraphic unit	Porosity, Φ (–)	Permeability, k (m^2)	van Genuchten parameter, α (kg^{-1} m s^2)	van Genuchten parameter, m (–)	Residual liquid saturation, S_r (–)
Fill	0.21	4.52×10^{-12}	5.07×10^{-4}	0.18	0.07
Alluvium	0.20	9.67×10^{-12}	8.46×10^{-4}	0.31	0.13

Table 3 Average soil thermal properties for different materials from Farouki (1982) considered in simulations S3.2 and S3.2′

Hydrostratigraphic unit	Formation heat conductivity, CWET ($W\ m^{-1}\ °C^{-1}$)	Formation heat conductivity under desaturated conditions, CDRY ($W\ m^{-1}\ °C^{-1}$)	Rock grain specific heat, SPHT ($J\ kg^{-1}\ °C^{-1}$)
Atmosphere	0.025	0.025	1010
Fill	1.5	0.5	800
Alluvium	2.5	2	1000
Bedrock[a]	1.5	0.5	1×10^6

[a] An additional material at the bottom of the domain was added with an infinite specific heat to keep the bottom temperature constant at 12 °C

Table 4 Kinetic parameters for mineral dissolution/precipitation reactions[a]

Mineral	Neutral mechanism		Acid mechanism			Additional mechanism		
	k_{nu} (mol $kg_{H_2O}^{-1}\ m^{-2}\ s^{-1}$)	E_{nu} (kJ mol^{-1})	k_a (mol $kg_{H_2O}^{-1}\ m^{-2}\ s^{-1}$)	E_a (kJ mol^{-1})	x[b]	k_{ex} (mol $kg_{H_2O}^{-1}\ m^{-2}\ s^{-1}$)	E_{ex} (kJ mol^{-1})	Species involved, a_{ij}^y
Goethite[c]	1.15×10^{-8}	86.5						
Calcite[d]	1.55×10^{-6}	23.5	5.01×10^{-1}	14.4	1	3.31×10^{-4}	35.4	$[CO_3^{-2}]$
Siderite[e]	2.24×10^{-9}	48.0	1.79×10^{-4}	48.0	0.75			
Pyrite[f]	0.0	56.9				2.63×10^{-8}	56.9	$[Fe^{+3}]^{0.3}\cdot$ $[Fe^{+2}]^{-0.47}\cdot$ $[H^+]^{-0.32}$
						7.94×10^{-8}	56.9	$[O_2]^{0.5}\cdot$ $[H^+]^{-0.11}$
SOM[g]	1.0×10^{-10} [h]	72.3[i]						

[a] Rates are reversible (unless otherwise noted) and computed as $R_i = \left[k_{nu} + k_a a_H^x + \sum_i k_{ex} \prod_j a_{ij}^y \right](1 - \Omega)$ with $k = k_{298.15}\ exp\ [- E/R\ (1/T — 1/298.15)]$

[b] Reaction order with respect to H^+

[c] Palandri and Kharaka (2004)

[d] Palandri and Kharaka (2004)

[e] Duckworth and Martin (2004)

[f] Williamson and Rimstidt (1994)

[g] Only dissolution is allowed

[h] Rate determined by the assumption of a non-limiting dissolved organic carbon (acetate) supply

[i] Davidson et al. (2012)

(Bosatta and Ågren 1995; Van Breukelen et al. 2004; Riley et al. 2014), for simplicity this study considers a single solid phase carbon source (cellulose) as the source of dissolved organic carbon at the site. This solid phase carbon will be henceforth referred to as SOM for Soil Organic Matter. SOM is assumed to react kinetically with the pore water, and is present in the model in amounts sufficient to provide an essentially unlimited supply of dissolved organic carbon in the form of acetate (Table 4):

$$C_6H_{10}O_5 + 2.5H_2O \rightarrow 3CH_3COO^- + 3H^+ \qquad (1)$$

Although simplistic, this representation of SOM and dissolved organic carbon has been used in other reactive transport studies (Hunter et al. 1998; Van Breukelen et al. 2004; Arora et al. 2015b), and it is considered sufficient here as a first-order, semi-quantitative approach to investigate the dominant controls on carbon dynamics at the site.

The microbially mediated redox reactions implemented in the simulations were based on previous studies at the site (Table 5). Several studies have documented iron and sulfate reduction to be important biogeochemical processes occurring at the Rifle site (Kukkadapu et al. 2010; Williams et al. 2011; Druhan et al. 2014a; Long et al. 2015). In addition, a field survey of the microbial populations indicated the presence and activity of chemolithoautotrophic bacteria (*Gallionella*, *Sulfurovum*, and *Sulfuricurvum*) responsible for the oxidation of Fe^{+2} and HS^- in reduced zones (Handley et al. 2013). Based on this information, chemolithoautotrophic pathways for the oxidation of Fe^{+2} and HS^- were explicitly represented in the reaction network (Fig. 2). These reactions were tested in various model simulations to evaluate their relative importance in affecting carbon fluxes at the site, with acetate being the source of chemical energy (Table 5). The biodegradation of acetate was coupled to several terminal electron acceptors, which follow the hierarchical sequence of aerobic respiration, nitrate reduction, iron reduction, and sulfate reduction. These biotic pathways were implemented using single Michaelis–Menten kinetics, and the sequence of TEAs was realized using inhibition terms that impede lower energy-yielding redox reactions when higher energy-yielding electron acceptors are present (e.g., Van Cappellen and Gaillard 1996; Doussan et al. 1997) (Table 6). It should be noted that the rate law parameters of the biotic reaction network considered here differ from those used in previous modeling studies at the site (e.g., Li et al. 2010; Druhan et al. 2014a) because the simulations cover a non-biostimulated zone. Hence, several orders of magnitude lower biodegradation rates are adopted. Characterizations of pore-water and solid phase chemistry at the site were used to calibrate some of the kinetic parameters given in Table 6. For simulations S3.2 and S3.2′, the temperature dependence of microbial reaction rate constants was also incorporated.

Table 5 Microbially mediated redox reactions and their thermodynamic parameters considered in the reactive transport model. See Table 6 for kinetic rate laws and parameters

Reaction stoichiometry	Rate Equation	$\log K$ (25 °C)[a]
Redox reactions with heterotrophic pathways		
$CH_3COO^- + 2O_2 \rightarrow 2HCO_3^- + H^+$	R_{O_2}	146.76
$CH_3COO^- + 4NO_3^- \rightarrow 2HCO_3^- + 4NO_2^- + H^+$	$R_{NO_3^-}$	89.04
$CH_3COO^- + 2.667NO_2^- + 1.667H^+ \rightarrow 2HCO_3^- + 1.33N_2 + 1.33H_2O$	$R_{NO_2^-}$	200.52
$NH_3(aq) + 2O_2 \rightarrow NO_3^- + H_2O + H^+$	R_{NH_3}	62.23
$CH_3COO^- + 8Fe^{+3} + 4H_2O \rightarrow 8Fe^{+2} + 2HCO_3^- + 9H^+$	$R_{Fe^{+3}}$	79.0
$CH_3COO^- + SO_4^{-2} \rightarrow 2HCO_3^- + HS^-$	$R_{SO_4^{-2}}$	8.40
Redox reactions with chemolithoautotrophic pathways		
$0.5HS^- + O_2 \rightarrow 0.5H^+ + 0.5SO_4^{-2}$	$R_{O_2-HS^-}$	68.90
$Fe^{+2} + 0.25O_2 + H^+ \rightarrow Fe^{+3} + 0.5H_2O$	$R_{O_2-Fe^{+2}}$	8.47
$HS^- + 1.6NO_3^- + 0.6H^+ \rightarrow SO_4^{-2} + 0.8N_2 + 0.8H_2O$	$R_{NO_3^--HS^-}$	11.52
$Fe^{+2} + 0.2NO_3^- + 1.2H^+ \rightarrow Fe^{+3} + 0.1N_2 + 0.6H_2O$	$R_{NO_3^--Fe^{+2}}$	−7.32

[a] Calculated from $\log K$ values for half redox reactions reported by Morel and Hering (1993)

Table 6 Kinetic rate laws and parameters for redox reactions

Rate law	Rate law parameters[a]	Reference
$R_{O_2} = K_{\max}^{O_2} \frac{[O_2]}{[O_2]+K_s^{O_2}}$	$K_{\max}^{O_2}(s^{-1}) = 5 \times 10^{-12}$	Calibrated[b]
	$K_s^{O_2}(molal) = 2.41 \times 10^{-5}$	Maggi et al. (2008)
	$E_a^{O_2}(KJ/mol) = 50$	Thamdrup et al. (1998)
$R_{NO_3^-} = K_{\max}^{NO_3^-} \frac{[NO_3^-]}{[NO_3^-]+K_s^{NO_3^-}} \frac{K_{O_2}^{in}}{K_{O_2}^{in}+[O_2]}$	$K_{\max}^{NO_3^-}(molal) = 2 \times 10^{-10}$	Parkhurst and Appelo (1999)
	$K_s^{NO_3^-}(molal) = 1.13 \times 10^{-4}$	Maggi et al. (2008)
	$K_{O_2}^{in}(molal) = 1.61 \times 10^{-8}$	Widdowson et al. (1988)
	$E_a^{NO_3^-}(KJ/mol) = 68$	McKenney et al. (1984)
$R_{NO_2^-} = K_{\max}^{NO_2^-} \frac{[NO_2^-]}{[NO_2^-]+K_s^{NO_2^-}} \frac{K_{O_2}^{in}}{K_{O_2}^{in}+[O_2]}$	$K_{\max}^{NO_2^-}(molal) = 3 \times 10^{-8}$	Calibrated[c]
	$K_s^{NO_2^-}(molal) = 1.13 \times 10^{-4}$	Maggi et al. (2008)
	$K_{O_2}^{in}(molal) = 1.61 \times 10^{-8}$	Widdowson et al. (1988)
	$E_a^{NO_2^-}(KJ/mol) = 30$	Wang et al. (1995)
$R_{NH_3} = K_{\max}^{NH_3} \frac{[NH_3]}{[NH_3]+K_s^{NH_3}} \frac{[O_2]}{[O_2]+K_s^{O_2}}$	$K_{\max}^{NH_3}(s^{-1}) = 5.27 \times 10^{-4}$	Calibrated[c]
	$K_s^{NH_3}(molal) = 1.48 \times 10^{-5}$	Wu et al. (2011)
	$K_s^{O_2}(molal) = 2.41 \times 10^{-5}$	Maggi et al. (2008)
	$E_a^{NH_3}(KJ/mol) = 87.1$	Kim et al. (2008)
$R_{Fe^{+3}} = K_{\max}^{Fe^{+3}} \frac{K_{O_2}^{in}}{K_{O_2}^{in}+[O_2]} \frac{K_{NO_3}^{in}}{K_{NO_3}^{in}+[NO_3^-]}$[d]	$K_{\max}^{Fe^{+3}}(s^{-1}) = 1 \times 10^{-13}$	Calibrated[e]
	$K_{O_2}^{in}(molal) = 1.61 \times 10^{-8}$	Widdowson et al. (1988)
	$K_{NO_3^-}^{in}(molal) = 1 \times 10^{-7}$	Doussan et al. (1997)
	$E_a^{Fe^{+3}}(KJ/mol) = 100$	Arndt et al. (2013)
$R_{SO_4^{-2}} = K_{\max}^{SO_4} \frac{[SO_4^{-2}]}{[SO_4^{-2}]+K_s^{SO_4}} \frac{K_{O_2}^{in}}{K_{O_2}^{in}+[O_2]} \frac{K_{NO_3}^{in}}{K_{NO_3}^{in}+[NO_3^-]}$ $\frac{K_{Fe}^{in}}{K_{Fe}^{in}+[Fe^{+3}]}$	$K_{\max}^{SO_4^{-2}}(s^{-1}) = 3 \times 10^{-12}$	Calibrated[f]
	$K_s^{SO_4^{-2}}(molal) = 1 \times 10^{-3}$	Li et al. (2010)
	$K_{O_2}^{in}(molal) = 1.61 \times 10^{-8}$	Widdowson et al. (1988)
	$K_{NO_3^-}^{in}(molal) = 1 \times 10^{-7}$	Doussan et al. (1997)
	$K_{Fe^{+3}}^{in}(molal) = 1 \times 10^{-12}$	Calibrated[g]
	$E_a^{SO_4^{-2}}(KJ/mol) = 77.5$	Amos et al. (2004)
$R_{O_2-HS^-} = K_{\max}^{O_2-HS^-} \frac{[HS^-]}{[HS^-]+K_s^{HS^-}} \frac{[O_2]}{[O_2]+K_s^{O_2}}$	$K_{\max}^{O_2-HS^-}(s^{-1}) = 2.38 \times 10^{-8}$	Luther et al. (2011)
	$K_s^{HS^-}(molal) = 1 \times 10^{-5}$	Handley et al. (2013)
	$K_s^{O_2}(molal) = 2.41 \times 10^{-5}$	Maggi et al. (2008)
	$E_a^{O_2-HS^-}(KJ/mol) = 65$	Ahonen and Tuovinen (1990)
$R_{O_2-Fe^{+2}} = K_{\max}^{O_2-Fe^{+2}} \frac{[Fe^{+2}]}{[Fe^{+2}]+K_s^{Fe^{+2}}} \frac{[O_2]}{[O_2]+K_s^{O_2}}$	$K_{\max}^{O_2-Fe^{+2}}(s^{-1}) = 5.25 \times 10^{-11}$	Calibrated[e]
	$K_s^{Fe^{+2}}(molal) = 1 \times 10^{-5}$	Mayer et al. (2002)
	$K_s^{O_2}(molal) = 2.41 \times 10^{-5}$	Maggi et al. (2008)
	$E_a^{O_2-Fe^{+2}}(KJ/mol) = 30.9$	Oba and Poulson (2009)
$R_{NO_3^--HS^-} = K_{\max}^{NO_3^--HS^-} \frac{[HS^-]}{[HS^-]+K_s^{HS^-}} \frac{[NO_3^-]}{[NO_3^-]+K_s^{NO_3^-}}$ $\frac{K_{O_2}^{in}}{K_{O_2}^{in}+[O_2]}$	$K_{\max}^{NO_3^--HS^-}(s^{-1}) = 7 \times 10^{-8}$	[h]
	$K_s^{HS^-}(molal) = 1 \times 10^{-5}$	Handley et al. (2013)
	$K_s^{NO_3^-}(molal) = 1.13 \times 10^{-4}$	Maggi et al. (2008)
	$K_{O_2}^{in}(molal) = 1.61 \times 10^{-8}$	Widdowson et al. (1988)
	$E_a^{NO_3^--HS^-}(KJ/mol) = 65$	[i]

Table 6 continued

Rate law	Rate law parameters[a]	Reference
$R_{NO_3^- - Fe^{+2}} = K_{\max}^{NO_3^- - Fe^{+2}} \dfrac{[Fe^{+2}]}{[Fe^{+2}] + K_s^{Fe^{+2}}} \dfrac{[NO_3^-]}{[NO_3^-] + K_s^{NO_3^-}}$ $\dfrac{K_{O_2}^{in}}{K_{O_2}^{in} + [O_2]}$	$K_{\max}^{NO_3^- - Fe^{+2}}(s^{-1}) = 7 \times 10^{-8}$ $K_s^{Fe^{+2}}(molal) = 1 \times 10^{-5}$ $K_s^{NO_3^-}(molal) = 1.13 \times 10^{-4}$ $K_{O_2}^{in}(molal) = 1.61 \times 10^{-8}$ $E_a^{NO_3^- - Fe^{+2}}(KJ/mol) = 22$	Palmer et al. (2010) Mayer et al. (2002) Maggi et al. (2008) Widdowson et al. (1988) Westerhoff (2003)

[a] For simulation S3.2, the rate constant is temperature-dependent and dynamically calculated as $K_{\max} = K_{25} \exp\left[\frac{-E_a}{R}\left(\frac{1}{T} - \frac{1}{298.15}\right)\right]$ where E_a is the activation energy

[b] Lowered by three orders of magnitude starting from the value in Russell (1973), to yield computed Fe^{+2} concentrations close to measured values while maintaining pyrite oxidation in the system

[c] Adjusted from Maggi et al. (2008) so as to drive the redox zonation to iron/sulfate reduction while not de-stabilizing the system with overly fast reaction rates

[d] Assumes an unlimited Fe^{+3} supply (from abundant solid Fe hydroxides)

[e] Calibrated to stabilize pH in groundwater close to measured values

[f] Adjusted several orders of magnitude lower than the values reported by Li et al. (2010) and Druhan et al. (2014a) for acetate-amended experiments

[g] Adjusted to yield background dissolved Fe^{+2} concentrations reasonably close to measured values

[h] Kept to yield similar maximum reaction rate as R_{NO3-Fe}^{-+2}

[i] Kept to yield similar activation energy as R_{O2-HS}^-

It should be noted that the inorganic reaction system is coupled to the biotic reaction network through the kinetic constraints on the multiple TEAs used by the simulated microbial consortium that includes heterotrophs and chemolithoautotrophs. Thus, the stoichiometries of redox sensitive aqueous species and minerals are decoupled in the input thermodynamic database and elements with different redox states are treated as separate primary variables i.e., as individual "basis" species (e.g., all Fe(III) minerals and aqueous species are written in terms of Fe^{+3}, all Fe(II) minerals in terms of Fe^{+2}).

Initial and boundary conditions

Following the conceptual model described above, fixed concentrations of dissolved species were applied at the top and left (up-gradient) model boundaries (Table 7). The fixed water composition at the up-gradient boundary was taken as that measured in well TT-01, and is considered representative of oxic recharge. The initial concentrations of (undetected) S(-2) and Fe(III) were set by equilibration with pyrite and goethite, respectively, and pH was recalculated to yield equilibrium with calcite, resulting in a pH consistent with field data (Table 7). For simplicity, the same water composition was also assumed for infiltration at the top model boundary, although in this case the infiltration water was re-equilibrated with atmospheric O_2 and CO_2 concentrations (Table 7).

The groundwater composition at well TT-01 contrasts with the composition at down-gradient well TT-03, which is suboxic and representative of the more reducing conditions within NRZs at the site. The composition of this more reduced water, also equilibrated with pyrite and goethite to yield initial concentrations of S(-2) and Fe(III), respectively, was chosen as initial conditions over the entire model domain (Table 7). The sediments throughout the entire domain were set with an initial mineral composition representative of NRZs (Table 8). The proxy SOM phase was given an equilibrium constant calculated to yield acetate concentrations (at equilibrium with this phase, Reaction 1) representative of measured concentrations (Table 7).

A closed (no-flux) bottom model boundary was applied to represent the top of the low permeability Wasatch formation. The first sets of simulations (S1, S2 and S3) were run with a fixed water table height and hydraulic gradient (April 2013; averaging 0.0025), maintained by fixed pressures at up-gradient and down-gradient boundaries, with the latter set at the

Table 7 Pore water compositions (molal) for initial and boundary conditions

Species	Left (oxic) boundary[a]	Top (oxic) boundary[a]	Concentration (molal) for (reduced) initial conditions[b]
pH	7.01[c]	7.99[c]	6.98[c]
Cl	6.08×10^{-3}	6.08×10^{-3}	2.57×10^{-3}
HCO$_3$	8.24×10^{-3}	7.80×10^{-4} [d]	9.53×10^{-3}
Al	3.48×10^{-6}	3.48×10^{-6}	9.74×10^{-10}
Ca	5.59×10^{-3}	5.59×10^{-3}	4.48×10^{-3}
Mg	6.16×10^{-3}	6.16×10^{-3}	4.06×10^{-3}
O$_2$ (aq)	7.83×10^{-6}	3.23×10^{-4} [e]	1.00×10^{-10} [f]
Fe(II)	7.49×10^{-5}	7.49×10^{-5}	7.85×10^{-5}
Fe(III)	6.15×10^{-13} [g]	3.74×10^{-13} [g]	6.28×10^{-13} [g]
K	3.48×10^{-4}	3.48×10^{-4}	2.00×10^{-4}
Na	1.25×10^{-2}	1.25×10^{-2}	7.56×10^{-3}
S(-2)	1.07×10^{-10} [h]	4.93×10^{-10} [h]	1.07×10^{-10} [h]
SO$_4$	1.18×10^{-2} [i]	1.48×10^{-2} [i]	6.94×10^{-3} [i]
SiO$_2$ (aq)	3.30×10^{-4}	3.30×10^{-4}	4.04×10^{-4}
NO$_3$	2.31×10^{-5}	2.31×10^{-5}	1.00×10^{-10} [f]
NO$_2$	1.05×10^{-6}	1.05×10^{-6}	1.00×10^{-10} [f]
N$_2$ (aq)	1.00×10^{-10} [f]	1.00×10^{-10}[f]	1.00×10^{-10} [f]
Acetate	1.00×10^{-10} [f]	1.00×10^{-10} [f]	9.94×10^{-4}
NH$_3$ (aq)	6.67×10^{-6}	6.67×10^{-6}	2.22×10^{-4}
P$_{CO2(12 \ °C)}$	0.028 bar	0.004 bar	0.035 bar

[a] Measured concentrations in pore water at TT-01 in May 2013, unless indicated otherwise

[b] Measured concentrations in pore water at TT-03 in May 2013, unless indicated otherwise

[c] Fixed by equilibrium with calcite

[d] Fixed by P$_{CO_2}$ (g) of $10^{-3.5}$ bar

[e] Fixed by P$_{O_2}$ (g) of $10^{-0.7}$ bar

[f] Small assumed value (below detection)

[g] Fixed by equilibrium with goethite

[h] Fixed by equilibrium with pyrite

[i] Adjusted for charge balance

average annual river level. These simulations were also run for a constant temperature (12 °C) representative of the mean measured aquifer temperature in April 2013. Because simulations S2 and S3 were restarted from S1, their initial conditions were taken from the inherited modeled state of simulation S1.

The second set of simulations (S3.1, S3.1′, S3.2, and S3.2′) were run to assess the effect of variable groundwater levels and subsurface temperatures on model results. For simulations S3.1 and S3.1′, a variable flux was imposed at the left boundary (at the edge of the model domain) to simulate observed water table fluctuations (Fig. 4). Heat flow was

considered in simulation S3.2 by imposing a vertical temperature gradient at the left model boundary and using soil thermal properties (Table 3) that were chosen to reproduce the maximum temperature gradient observed with depth in well TT-03 (Fig. 5). In contrast, to simulate observed temperature fluctuations with simulation S3.2′ (Fig. 5c), a variable heat boundary was imposed at the top of the model domain and a constant temperature of 12 °C was imposed along the bottom model boundary. For simulations S3.2 and S3.2′, the right model boundary corresponding to the river was kept at a constant 12 °C average temperature, and the location of the

Table 8 Initial mineral volume fractions considered in the simulations

Mineral	Density (g cm^{-3})	Molar volume (cm^3 mol^{-1})	Volume fraction (−)	Specific surface area ($m^2_{mineral}$ $m^{-3}_{mineral}$)[a]
Goethite	4.268	20.82	1.2×10^{-3} [b]	60,000
Calcite	2.710	36.934	0.01[c]	60,000
Siderite	3.944	29.378	4.09×10^{-3}[d]	60,000
Pyrite	5.012	23.94	3.6×10^{-5} [e]	60,000
SOM	1.500	108.059[f]	0.0626	1.13×10^5 [g]

[a] Reactive surface area are calculated assuming 100 micron spherical grains unless otherwise noted

[b] Based on 3.8×10^{-5} mol/g hydroxylamine-extractable Fe(III) content in fine grained (<2 mm) Rifle sediments (Li et al. 2010; Campbell et al. 2012)

[c] Assumed low value from visual observation of calcite in sediments

[d] Based on 0.5 M HCL Fe(II) content in fine grained (<2 mm) Rifle sediments (Campbell et al. 2012) yielding a value largely dominating the amount of Fe(II) sulfide in the sediment (see [e])

[e] Based on 7×10^{-7} mol/g acid volatile sulfide content in fine grained (<2 mm) Rifle sediments (Campbell et al. 2012)

[f] Fixed by density and molecular weight

[g] Based on the smallest particle size fraction (53 micron) with reported organic matter content in Rifle sediments (Campbell et al. 2012)

water table was kept constant as was the case for simulation S3.

Simulated cases

Base case simulation (S1)

The base case simulation was designed to consider abiotic reactions so as to gain insight into the interpretation of processes controlling the self-organization of naturally reduced zones associated with reduced Fe and S phases. In this study, several iron minerals (goethite, siderite, and pyrite) are associated with the sediments and can influence the redox cycling of Fe and S as well as affect C fluxes. For example, two independent and parallel pathways for pyrite dissolution are considered:

$$FeS_{2(s)} + 3.5O_2 + H_2O \rightarrow Fe^{+2} + 2SO_4^{-2} + 2H^+ \tag{2}$$

$$FeS_{2(s)} + 14Fe^{+3} + 8H_2O \rightarrow 15Fe^{+2} + 2SO_4^{-2} + 16H^+ \tag{3}$$
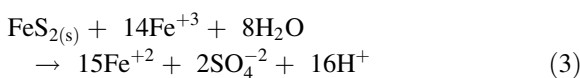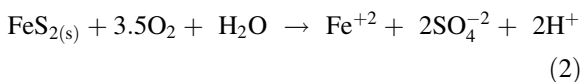
Because different rate laws are used for the two reactions (see Table 4), the overall pyrite dissolution reaction depends on whether Fe^{+3} or O$_2$(aq) is the dominant oxidant (Williamson and Rimstidt 1994;

Steefel 2000). The second pathway (Reaction 2) is coupled to the dissolution of goethite, which is modeled using a kinetic rate law (Table 4):

$$FeOOH_{(s)} + 3H^+ \rightarrow Fe^{+3} + 2H_2O \tag{4}$$
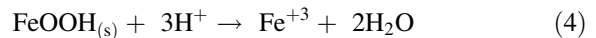
The overall effect of Reactions 3 and 4 yields the reductive dissolution of Fe^{+3} by sulfide:

$$FeS_{2(s)} + 14FeOOH_{(s)} + 26H^+ \rightarrow 15Fe^{+2} + 2SO_4^{-2} + 20H_2O \tag{5}$$
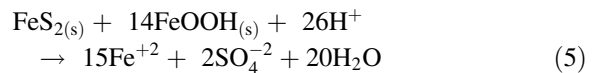
Among the minerals considered here, siderite and calcite dissolution directly affect CO$_2$ geochemistry:

$$FeCO_{3(s)} + H^+ \rightarrow Fe^{+2} + HCO_3^- \tag{6}$$

$$CaCO_{3(s)} + H^+ \rightarrow Ca^{+2} + HCO_3^- \tag{7}$$
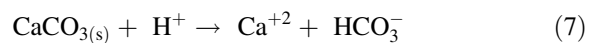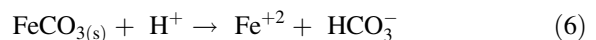
Note that Reaction 5 strongly affects pH, which indirectly impacts bicarbonate alkalinity through Reactions 6 and 7. Thus, for simulation S1, carbon fluxes and the spatial extent of the NRZ in the system are controlled by these mineral reactions only (with rates as listed in Table 4).

Simulation S1 was run for 15 years with a fixed water table height and fixed temperature (12 °C) until steady chemical conditions were reached that matched approximately the field observations. Note that a mean groundwater residence time of 6 years was computed from the model input parameters.
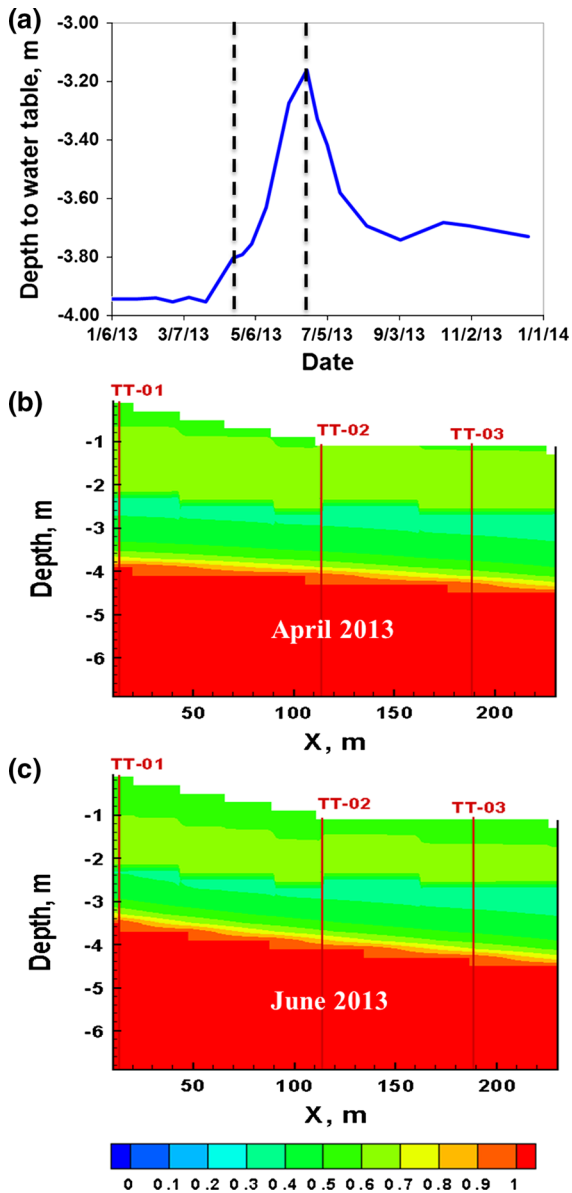
Fig. 4 a Time series of water table depth at a stilling well located upstream of the site, and **b**, **c** snapshots of simulated liquid saturation profiles for April and June 2013, respectively using S3.1. The dashed lines in **a** show the period of rising water table that was simulated in S3.1

Biotic with heterotrophic pathways (S2)

Biotic pathways for the degradation of acetate and CO_2 production (Table 5) were introduced in this simulation by restarting S1 and simulating for an additional 6 years. 6 years was sufficient to evolve to a quasi-steady state controlled by the balance between influxes
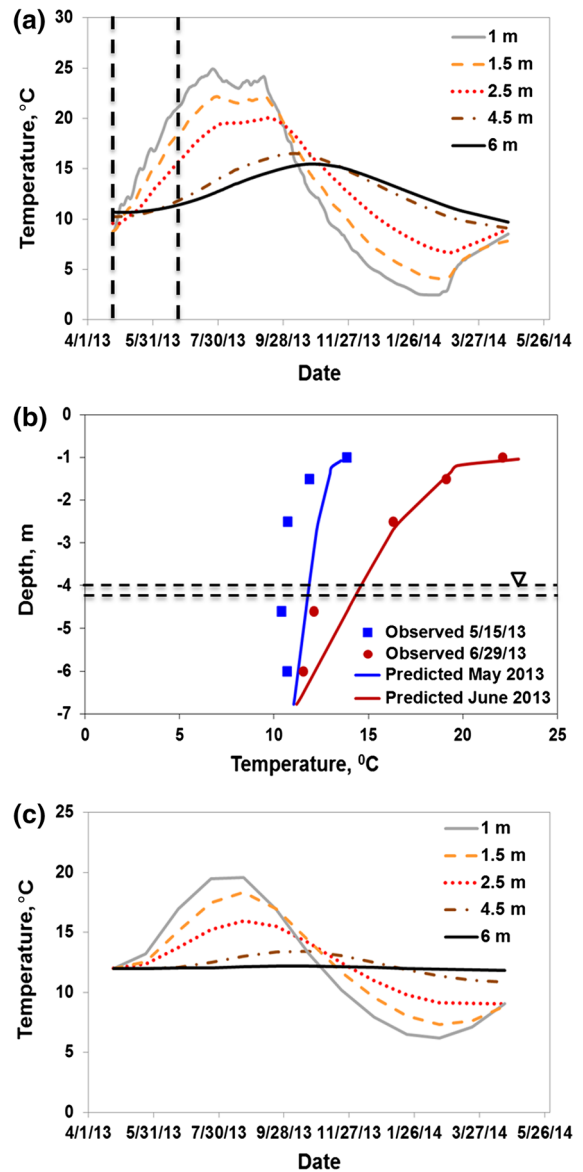
Fig. 5 a Time series of temperature data at TT-03—dashed lines show the April–June 2013 time frame considered in short-term simulations (Table 1), **b** snapshots of simulated temperature gradients for May and June 2013 using S3.2—*dashed lines* show the water table level in April (*low*) and June 2013 (*high*), and **c** simulated annual temperature fluctuations using S3.2′. *Note* that the depth on the y-*axis* corresponds to the modeled domain and not true ground surface

and heterotrophic respiration rates. In addition to reaction 5, the reductive dissolution of goethite is now simulated as the rate-limited microbial reduction of Fe^{+3} (Table 5) coupled with kinetic dissolution of goethite (Table 4), with the overall reaction given by:

$$8FeOOH_{(s)} + CH_3COO^- + 15H^+$$
$$\rightarrow 8Fe^{+2} + 2HCO_3^- + 12H_2O \qquad (8)$$
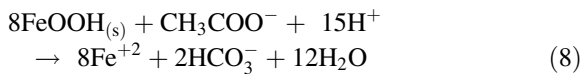
Note that reaction (8) also strongly affects pH and indirectly impacts bicarbonate alkalinity through reactions (6) and (7). Thus, for simulation S2, carbon fluxes and the spatial extent of the NRZ in the system are determined by both abiotic and biotic reactions.

Biotic reactions with chemolithoautotrophic pathways (S3)

Biotic reactions with both heterotrophic and chemolithoautotrophic pathways (Fig. 2) were introduced in this simulation by restarting S1 and simulating for an additional 6 years. A time frame similar to that of simulation S2 was chosen so as to clearly distinguish the contributions from chemolithoautotrophic processes. The aqueous concentrations are found to approach a quasi-steady state within this time frame. Therefore, in addition to the oxidation of acetate to CO_2 through several sequential pathways as in S2, oxygen- and nitrate-dependent oxidation of Fe^{+2} and HS^- were considered in this simulation ($R_{O2\text{-}HS}^-$, $R_{O2\text{-}Fe}^{+2}$, $R_{NO3\text{-}HS}^-$, $R_{NO3\text{-}Fe}^{+2}$, Table 5). Thus, for simulation S3, carbon fluxes and the spatial extent of the NRZ in the system depend on the tight coupling between transport, abiotic and biotic reactions as well as the biogeochemical recycling of SO_4^{-2} and Fe^{+3} through chemolithoautotrophic pathways.

Seasonal and annual water table fluctuations (S3.1 and S3.1′)

S3.1 and S3.1′ cases were derived directly from simulation S3 (with fixed water table conditions), except that water level fluctuations (Fig. 4) were included. Simulation S3.1 incorporates time-dependent boundary conditions to investigate the effect of seasonal water table variations (April–June 2013) on soil CO_2 concentrations at the site. Simulation S3.1′ was run for a full year cycle of water level fluctuations (January 2013–January 2014) to assess the impact of annual water table variations on groundwater carbon exports to the river. Water table fluctuations observed at a stilling well (located 0.4 miles from the southeast boundary, upstream of the site) for an entire year at the Rifle site are shown in Fig. 4a and two representative snapshots of the simulated saturation profiles at both low and high

water levels in April and June 2013 are shown in Fig. 4b, c, respectively. Thus, for simulations S3.1 and S3.1′, carbon fluxes in the system include the effect of water table fluctuations and the impact of these variations on abiotic and biotic reactions producing CO_2.

Temperature gradients (S3.2) and annual temperature fluctuations (S3.2′)

S3.2 and S3.2′ cases were also derived from simulation S3, except that heat transport driven by temperature changes (Fig. 5) was included. Simulation S3.2 incorporates the temperature difference between the top and bottom of the modeled domain and investigates the effect of temperature gradients observed in June 2013 on soil CO_2 concentrations at the site. Simulation S3.2′ was run for a full year cycle of temperature fluctuations (April 2013–April 2014) to assess the impact of annual temperature fluctuations on groundwater carbon exports to the river. In these cases, to clearly distinguish temperature effects from water level effects, the water table was kept at a constant level, as in simulation S3. In addition, the influence of temperature on abiotic and biotic processes was separately evaluated for each of these cases. Thus as with simulation S3.2, the simulated CO_2 dynamics are affected by temperature gradients during June 2013 (Fig. 5b) and in the case of simulation S3.2′, carbon fluxes are impacted by annual temperature fluctuations (Fig. 5c). It should be noted that an increase in temperature results in decreasing CO_2 solubility (increasing volatility), decreasing calcite solubility (retrograde behavior), and increasing kinetic rates of both abiotic and microbial reactions.

Results and discussion

Results are presented for the two sets of simulations discussed above—the first set (S1, S2 and S3) focuses on understanding the relative contribution of different abiotic and biotic reactions on soil CO_2 concentrations under conditions of constant water table depth and temperature; the second set of simulations (S3.1 and S3.2) is used to evaluate CO_2 dynamics under conditions of variable water levels and subsurface temperatures. Groundwater carbon exports from the site to the river are evaluated using both sets of simulations (S1, S2, S3, S3.1′, and S3.2′).

Simulated liquid saturation and biogeochemical trends

Simulated liquid saturation profiles from S1 (S2 or S3 could also have been used) were compared with data derived from neutron probe measurements under steady water table conditions (March 2014) at wells TT-01, TT-02 and TT-03 (Fig. 6). It should be noted that the neutron probe readings were likely affected by bentonite, which was used as backfill material for the surface-most regions (up to ~0.9 m) of the TT wells, and for this reason no attempt was made to calibrate precisely flow model parameters to these data. To provide additional and likely better-constrained "observations", liquid saturation profiles at well TT-03 were also estimated by fitting laboratory-determined van Genuchten parameters to tensiometer readings (March 2014) at various depths in this well (Fig. 6c). Figure 6 reveals a discontinuity in both the measured and simulated saturation profiles at the fill-alluvium interface (brown dotted lines) for all wells. Below the fill materials, the simulations capture reasonably well the trend of liquid saturations derived from these measurements; within the fill, the model appears to underestimate liquid saturation slightly, particularly in the shallower part of the modeled domain where bentonite was used. Note that this underestimation of the liquid saturation (if real) can affect the computed value of the gas diffusion coefficient (through the Millington-Quirk tortuosity formulation) and result in a system that is more open to gas flow, as discussed in the next section.

The conceptual model of NRZ persistence at the site was tested by comparing the predicted spatial distribution of important redox-sensitive species for the different modeled simulations: abiotic (simulation S1), biotic with heterotrophic (simulation S2) and chemolithoautotrophic pathways (simulation S3) (Fig. 7). Figure 7a shows that with simulation S1, oxidizing conditions develop in the vadose zone (as would be expected), whereas slightly reducing conditions are predicted to remain in the saturated zone. In this case, steady state redox conditions are determined by abiotic pathways alone and are controlled by the mass fluxes of redox species at the recharge boundary and the rates of mineral precipitation/dissolution reactions (e.g., reactions 5–7). Under this scenario, the reducing conditions initially imposed throughout
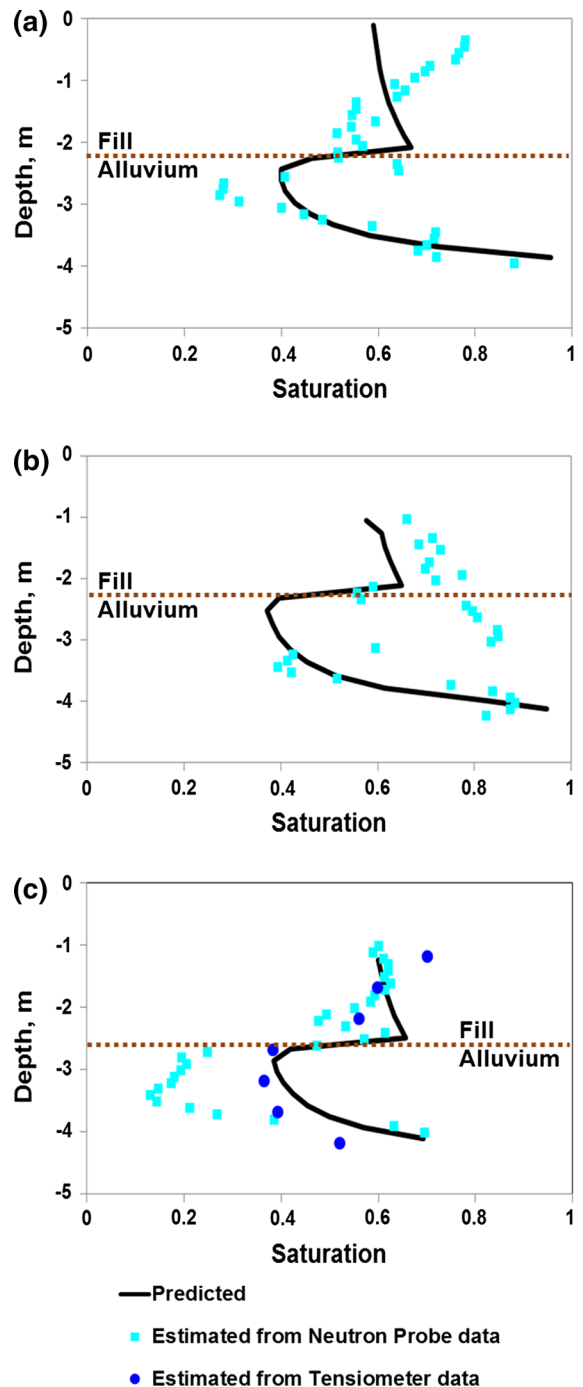
Fig. 6 Simulated and observed profiles of saturation versus depth at wells **a** TT-01, **b** TT-02, and **c** TT-03. A consistent calibration of volumetric water content (VWC) = 0.50*counts ratio −0.05 was used at all 3 wells for the neutron probe measurements. *Note* that the depth on the y-axis corresponds to the modeled domain and not true ground surface
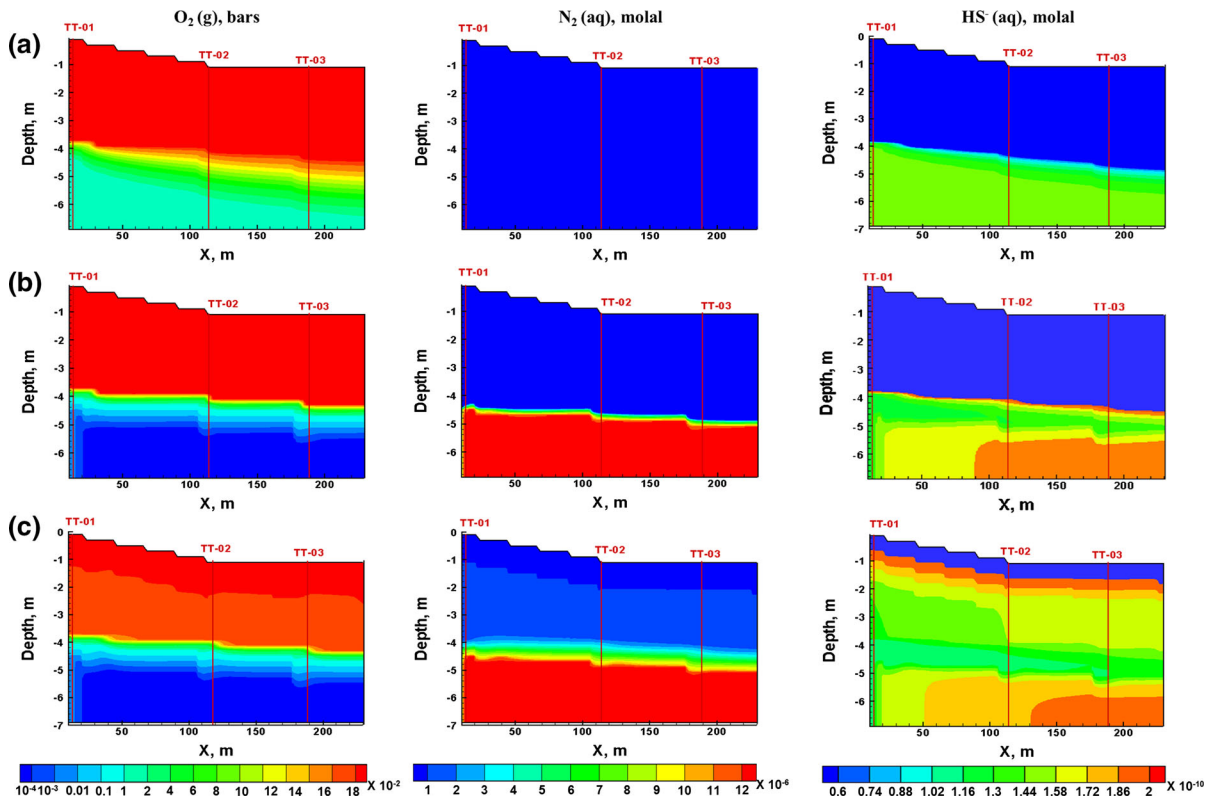
Fig. 7 Simulated spatial distributions of O$_2$(g), N$_2$(aq) and HS$^-$(aq) along the TT transect using **a** abiotic, **b** abiotic + biotic with heterotrophic pathways, and **c** abiotic + biotic with both heterotrophic and chemolithoautotrophic pathways. The NRZ persists closer to the river when chemolithoautotrophs are taken into account

the model domain cannot be maintained at steady state, as shown with the simulated profiles for dissolved O$_2$, N$_2$ and HS$^-$ (Fig. 7a). Note that the computed HS$^-$ concentration in the presence of O$_2$ is essentially zero. Evolving from these conditions, a redox zonation develops in the saturated zone when microbial reactions are considered in simulations S2 and S3 (Fig. 7b, c). In the vadose zone, oxidizing conditions are predicted to prevail with simulation S2 but not with S3. In the saturated zone, oxygen is depleted at a more rapid pace with both simulations S2 and S3 through the different microbially mediated pathways (Fig. 2). With simulations S2 and S3, denitrifying conditions cannot be maintained in the saturated zone because of the rapid rate of nitrate reduction through biotic pathways (Fig. 7b, c). Some elevated N$_2$ concentrations are also observed in the vadose zone with simulation S3. In both cases, the predicted sulfide concentration (HS$^-$) increases in the

down-gradient portion of the cross section as a result of the interplay between the rate of dissolution of pyrite, heterotrophic reduction, and in S3, chemolithoautotrophic oxidation of iron and sulfide (Table 5) (Fig. 7b, c). When only heterotrophic processes are considered (Fig. 7b), the observed persistence of the NRZ near the river (right model boundary) cannot be reproduced as well as when chemolithoautotrophic oxidation is also included (Fig. 7c). This suggests that chemolithoautotrophic processes not only increase O$_2$ and NO$_3^-$ depletion, but also promote further heterotrophic reduction of Fe^{+3} and SO$_4^{-2}$ through the cycling of these redox species. Thus, these processes control the spatial redox zoning observed in the saturated zone. An increase in acetate concentration in the down-gradient portion of the cross section in the case of both simulations S2 and S3 is further observed (not shown here). The lateral distribution of acetate also appears to be controlled by

the influx of up-gradient oxic recharge and microbial reactions.

These results suggest that abiotic pathways alone cannot account for the redox zonation observed at the site in the form of NRZs. The spatial extent of reduced zones near well TT-03 can be obtained by controlling the interactions between oxidizing recharge and homogeneous flood plain sediments, but more importantly by considering chemolithoautotrophic processes through the redox cycling of Fe^{+3} and SO_4^{-2}.

CO_2 concentrations from abiotic and multiple biotic pathways

2-D model simulations were used further to evaluate the effect of the different biogeochemical pathways on CO_2 efflux from the site. In the saturated zone, the transport of CO_2 (inorganic carbon) is dominated by advection, whereas CO_2 fluxes in the vadose zone are primarily diffusive (although advective effects from barometric pumping and/or water table fluctuations cannot be ruled out completely). The CO_2 partial pressure in groundwater at the water table (computed from the compositions shown on Table 7, reflecting equilibrium with calcite as suggested by field observation) is elevated and varies around 0.03 bar ($\sim$30,000 ppmV) in the range of groundwater temperatures recorded at the site (Fig. 8). Thus, the

flux of CO_2 in the vadose zone depends not only on microbial activity above the water table, but also on the significant gradient between the elevated CO_2 concentrations at the water table and the low atmospheric values above ground ($\sim$400 ppmV). The CO_2 diffusion across this gradient is a function of liquid saturation (through the tortuosity factor, Figure A-1), which in this case lowers the diffusive flux (compared to a fully gas-saturated system) by about 1 order of magnitude at the lowest modeled liquid saturation ($\sim$0.4, Fig. 6), and significantly more so at higher liquid saturations (Figure A-1). Therefore, variations in liquid saturation alone (such as from a rising water table and/or rainfall events) are expected to significantly affect the CO_2 diffusive flux and spatial variability of CO_2 concentrations in the vadose zone.

Figure 9 compares simulated steady state CO_2 concentrations at TT-01, TT-02, and TT-03 wells for the three simulated cases: abiotic (S1), biotic with heterotrophic (S2) and chemolithoautotrophic pathways (S3) with observed profiles. Because water table conditions were stable in the beginning of April 2013, CO_2 measurements from this month were used for comparison. Note that observed CO_2 concentrations for April 2014 are shown for reference only and not used in this analysis because hydrological conditions in 2014 were significantly different from 2013. Figure 9 clearly demonstrates that both simulations S1 and S2 predict relatively low P_{CO2} in the vadose zone that are far from observations. In the saturated zone, simulation S2 results in higher P_{CO2} than S1 as a result of heterotrophic respiration. The inclusion of chemolithoautotrophic processes further increases the predicted CO_2 concentration in the deeper vadose zone (around 3 m), where higher volume fractions of CO_2 are generally observed. Simulation S3 reproduces observed CO_2 profiles better than the other simulated cases in both wells TT-01 and TT-02. However, simulation S3 still underestimates observed CO_2 concentrations particularly at well TT-03 where CO_2 concentrations are elevated and generally higher than those observed at TT-01 or TT-02. As discussed below, temperature has an important effect on CO_2 concentrations and inclusion of the observed temperature gradients in the simulations significantly improves the match of the observations and predictions.

Simulated and observed profiles of pH, HCO_3^-, and acetate concentrations at well TT-02 are presented
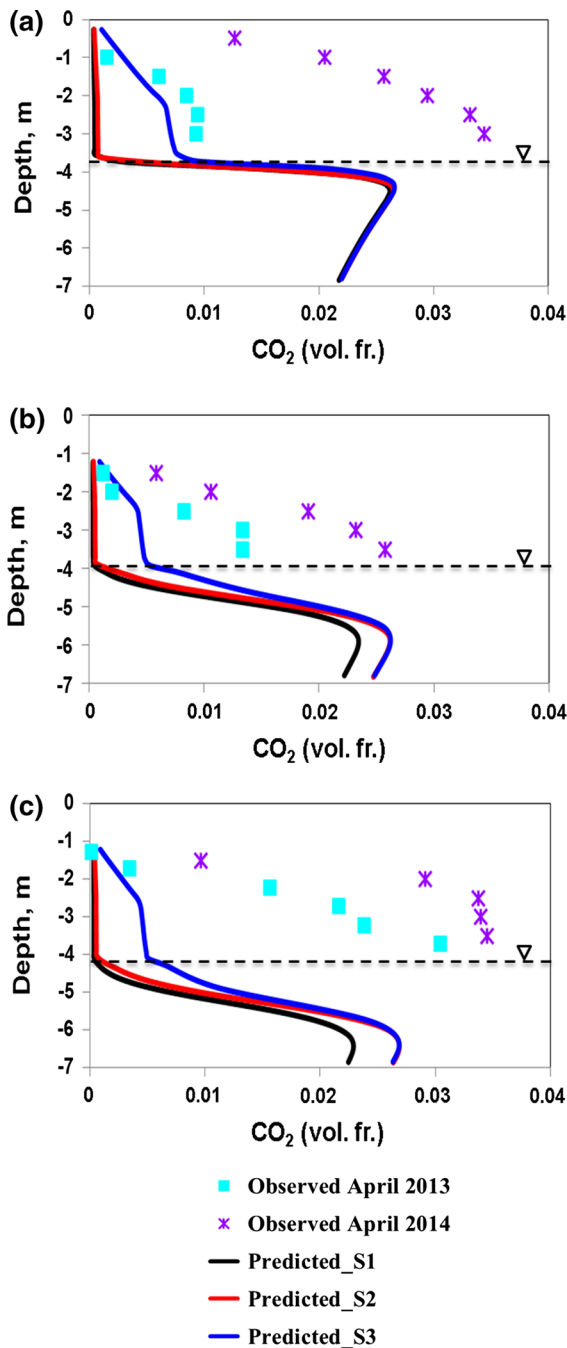

Fig. 8 Computed CO_2 partial pressure in groundwater as a function of temperature at wells TT-01 and TT-03 (see Table 7 for the corresponding groundwater compositions), for a system buffered by equilibrium with calcite, which is observed at the site. The *shaded area* shows the typical range of temperature in the saturated and deep vadose zone at the site (see Fig. 5)

Fig. 9 Simulated and observed profiles of $CO_2(g)$ volume fraction versus depth at wells **a** TT-01, **b** TT-02, and **c** TT-03 for three modeled cases (S1, abiotic; S2, abiotic + biotic with heterotrophic pathways; and S3, abiotic + biotic with both heterotrophic and chemolithoautotrophic pathways). *Note* that the depth on the y-*axis* corresponds to the modeled domain and not true ground surface. (Color figure online)
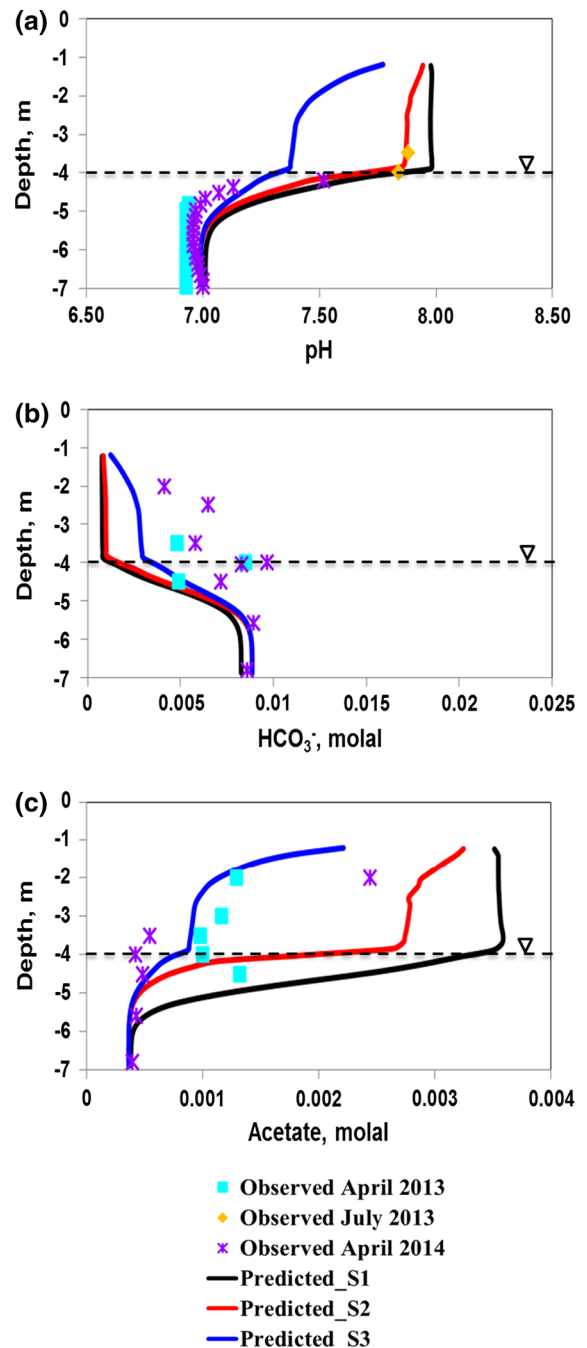
Fig. 10 Simulated and observed profiles of pH, total dissolved carbonate concentration (as HCO_3^-), and acetate concentration versus depth at well TT-02 for three modeled cases (S1, abiotic; S2, abiotic + biotic with heterotrophic pathways; and S3, abiotic + biotic with both heterotrophic and chemolithoautotrophic pathways). *Note* that the depth on the y-*axis* corresponds to the modeled domain, and pH measurements in the vadose zone (*orange diamonds*) were confined to one sampling event in July 2013. (Color figure online)

in Fig. 10. Again, a comparison between simulated and observed profiles is carried out for April 2013 and observations for April 2014 are shown for reference only. Simulations S2 and S3 predict lower pH values in the vadose zone as compared to S1 (Fig. 10a). This is expected as several biotic pathways including microbially mediated breakdown of acetate cause a decrease in pH (R_{O2}, R_{NO3}^-, R_{Fe}^{+3}, R_{SO4}^{-2}, R_{NH3}, Table 5). The lower pH by itself would result in a lower bicarbonate concentration. However, in this case the biotic reactions yield an increase in dissolved carbonate concentration (Fig. 10b), and more so for simulation S3 than for S2. Although chemolithoautotrophic reactions (R_{O2-HS}^-, R_{NO3-HS}^-, R_{O2-Fe}^{+2}, R_{NO3-Fe}^{+2}, Table 5) do not directly contribute to this increase, the redox cycling of Fe and S and a resulting increase in the breakdown of acetate can lead to higher dissolved carbonate concentrations. A decrease in acetate concentration is clearly visible in the vadose zone for simulation S3 (Fig. 10c). In the saturated zone, the simulated acetate concentration with S3 is also lower than obtained with S1 and S2. These vertical acetate profiles are governed by two controlling processes—one, the microbially mediated breakdown that occurs when its concentration is high and in the presence of TEAs, and two, its release from SOM when its concentration is low.

Figure 9 clearly demonstrates that higher CO_2 concentrations are observed locally at TT-03, which is located within the NRZ. The simulations show an improved agreement with observations when both biotic heterotrophic and chemolithoautotrophic pathways, in addition to abiotic processes, are considered. Thus, simulation S3 will be used for evaluating the CO_2 dynamics under varying water table and temperature conditions at the site.

CO_2 concentrations under seasonal water table and temperature variations

Figure 11 shows simulated and observed profiles of $CO_2(g)$ volume fraction, pH, and HCO_3^- concentration between April and June 2013. Note that the water table rises and temperature increases during this time period (Figs. 4, 5). The observations show a consistent increase in CO_2 volume fractions in the vadose zone from April (blue squares) to May (pink triangles) to June 2013 (green circles) at all three wells. A slight increase in pH from May to June is also observed at all wells. Note that the trend of increasing pH with depth below the water table is observed only in well TT-03. The total dissolved carbonate concentration shows a slight increase below the water table at wells TT-01 and TT-02, but decreases from May to June at TT-03.

Evolving from the simulated steady water table conditions of S3 (blue solid lines) that are representative of April 2013, S3.1 predicts CO_2 production under rising water table conditions (green dashed lines) for June 2013. The simulations shown in Figs. 11a, c estimate a higher partial pressure of CO_2 at TT-01 than TT-03 below the water table (at matching depths), which seems to be related to the difference in water table rise at these two locations (a 0.6 m rise at TT-01 compared to only 0.1 m rise at TT-03; Fig. 4b, c). As discussed above, gas diffusivity decreases sharply with increasing liquid saturations (through the effect of tortuosity, Figure A-1), thus allowing more retention of CO_2 as the water table rises. Although simulation S3.1 is a realistic representation of the up-gradient recharge at the site, the simulated CO_2 profiles are not able to capture the observed increase in volume fraction of CO_2 between April and June 2013 for any of the wells.

Simulation S3.2, which considers a gradient of decreasing temperatures with depth (Fig. 5b), estimates CO_2 concentrations (green dotted lines) that are significantly higher than those obtained with simulation S3.1 and are closer to observed concentrations in June (green circles) at both TT-01 and TT-02 wells. However, this simulation considers temperature dependence on only abiotic reactions and still underestimates observed concentrations of CO_2 at well TT-03. The inclusion of temperature effects on microbially mediated reaction rates (green dash-dot lines) leads to a significant improvement in the estimation of CO_2 concentrations, particularly at TT-03 where a field survey of the microbial populations has confirmed the presence and activity of chemolithoautotrophic bacteria. Both observed and simulated CO_2 concentrations suggest that abiotic processes alone may be important drivers of seasonal CO_2 variability at wells TT-01 and TT-02, with temperature playing an important role on abiotic reaction rates but also on the solubility of CO_2. As noted above, the partial pressure of CO_2 derived from total dissolved (inorganic) carbon in
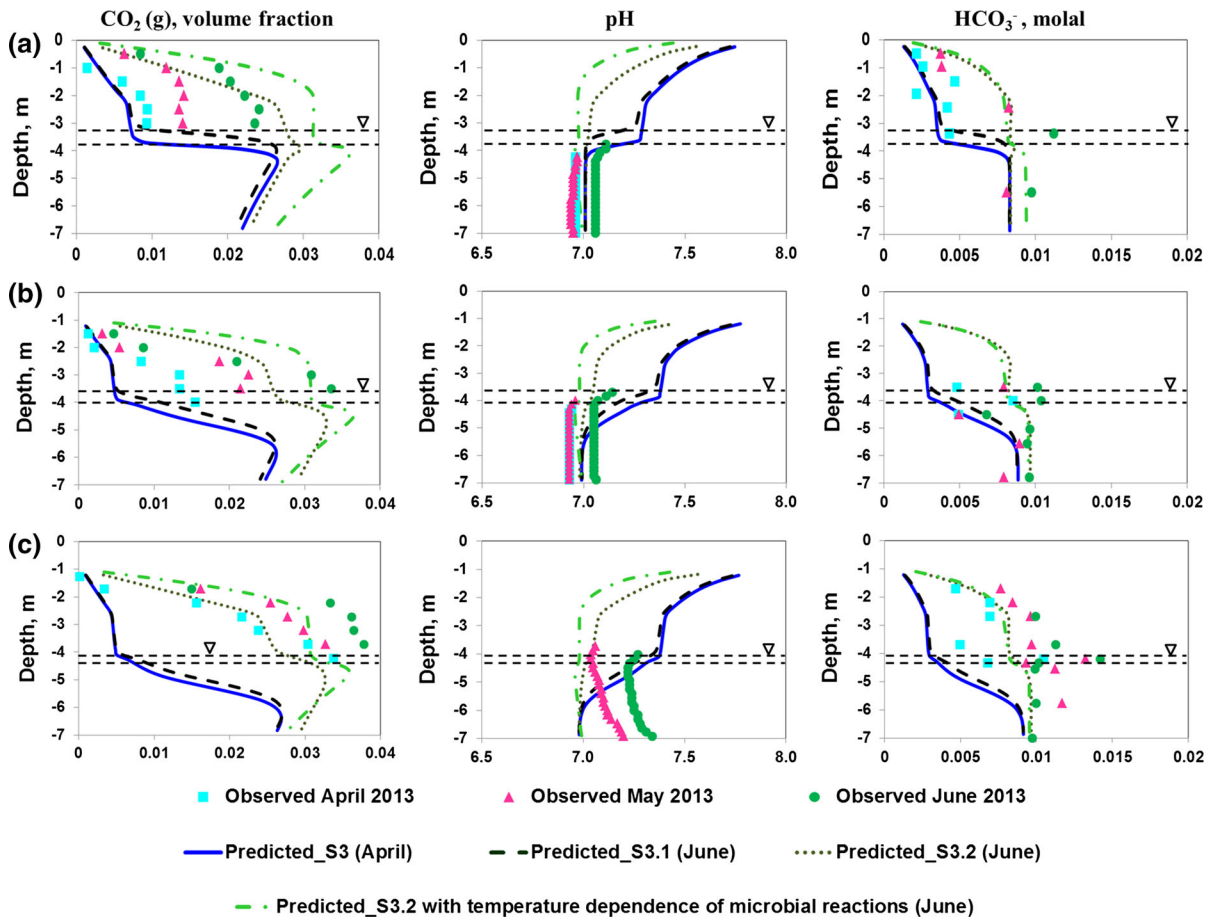
Fig. 11 Simulated and observed profiles of $CO_2(g)$ volume fraction, pH, and total dissolved carbonate concentration (as HCO_3^-) versus depth at wells **a** TT-01, **b** TT-02, and **c** TT-03 for three modeled cases all considering abiotic + biotic with both heterotrophic and chemolithoautotrophic pathways and S3, constant water levels and temperature; S3.1, adding water table fluctuations; and S3.2 adding temperature gradients. Observations for May 2013 are shown for reference only. *Note* that the depth on the y-*axis* corresponds to the modeled domain, and pH measurements in the vadose zone were not available during this time frame

groundwater at the water table is by itself a significant contributor of CO_2 to the vadose zone and is significantly impacted by temperature (Fig. 8). Figure 11 further suggests that the observed total dissolved carbonate concentrations and pH profiles are captured reasonably well by simulation S3.2 (green dash-dot lines) at all wells.

These results suggest that seasonal variability in CO_2 efflux at up-gradient locations within the site (TT-01, TT-02) is governed by abiotic processes, while a large efflux from the down-gradient location is a function of both microbially mediated processes and temperature controls. These results highlight the fact that CO_2 fluxes at a relatively small flood plain site ($\sim 90{,}000$ m^2) can show significant spatiotemporal variations. Capturing these variations in a model requires adequate process representation including site-specific microbial reactions and reactive transport in both aqueous and gas phases under non-isothermal and variably saturated conditions.

Annual carbon fluxes

Here we focus on subsurface CO_2 fluxes because these are typically neglected in carbon cycling studies on the basis that they are much lower than atmospheric fluxes

Table 9 Annual groundwater carbon exports to the river

Simulation	Dissolved inorganic carbon export, $(g\ m^{-2}\ d^{-1})$	Dissolved organic carbon export, $(g\ m^{-2}\ d^{-1})$
S1	1.208	0.048
S2	1.210	0.042
S3	1.212	0.042
S3.1′	1.210	0.041
S3.2′ (with temperature dependence of only abiotic processes)	3.265	0.121
S3.2′ (with temperature dependence of abiotic and biotic processes)	3.303	0.342

(Pulliam 1992; Raymond et al. 2000; Richey et al. 2002). Table 9 shows computed groundwater exports of inorganic and organic carbon to the river from the site along the TT transect based on the modeling described here (Simulations S1, S2, S3, S3.1′, and S3.2′). Note that for these calculations, simulations S3.1′ and S3.2′ were run for an entire year to capture the effect of annual water table and temperature variations. Again, a distinction between temperature impacts on abiotic and biotic processes is made in the table. These subsurface exports were computed as the product of the groundwater flow velocity and acetate or bicarbonate concentration at the down-gradient model boundary. For comparison, diffusive fluxes of CO_2 into the atmosphere at the top model boundary were also derived from the modeled CO_2 concentrations in the vadose zone. However, it should be noted that these fluxes do not include effects of plant respiration and transpiration, which for simplicity are not modeled here. These computed CO_2 fluxes to the atmosphere are significantly greater (8.24 kg $m^{-2}\ d^{-1}$ using S3.2′) than subsurface carbon exports (Table 9) and within the ranges reported for other flood plain sites (Billings et al. 1998; Batson et al. 2015).

Table 9 shows that inorganic carbon exports are at least an order of magnitude greater than organic carbon exports to the river for both steady and transient conditions. Ignoring the biotic pathways (S2 or S3 versus S1) leads to an overestimation of only 12 % in dissolved organic carbon exports to the river; however, the contribution of biotic pathways to atmospheric CO_2 fluxes is almost 230 %. Table 9 further demonstrates a decrease in inorganic carbon export and no change in organic carbon export when annual water table fluctuations are considered (S3.1′)
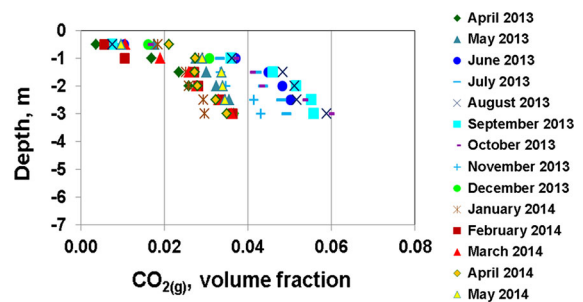
Fig. 12 Observed profiles of $CO_2(g)$ concentrations versus depth in the vadose zone at TT-03

as compared to steady water table conditions (S3). Thus, the annual wetting and drying events can have a cyclic effect and even decrease annual carbon fluxes from a given site. Certain studies also corroborate this decrease in groundwater carbon export due to water table fluctuations (Kim et al. 2012, and references therein). On the other hand, incorporation of annual temperature variations greatly increased groundwater carbon exports to the river. An increase of almost 150 % in both inorganic and organic carbon fluxes was obtained when considering temperature fluctuations and their impact on abiotic processes only (e.g., CO_2 solubility) as compared to the base case simulation (S1) in which a constant temperature was assumed. A three-fold increase in organic carbon was further obtained when temperature dependence on microbially mediated reactions was included. Figure 12 shows observed annual CO_2 concentration in the vadose zone at TT-03. It is clearly evident that the highest CO_2 concentrations are obtained between June and November 2013, which is strongly correlated with warming temperature months rather than sporadic

precipitation events or the growing season (April–October). This monthly rise in CO_2 concentration between June and November 2013 is also observed at TT-01 and TT-02 (not shown here). These results clearly highlight that temperature variations exert an outsized control on subsurface carbon fluxes at the Rifle site.

Conclusions

This study demonstrates that the decoupling of different biogeochemical processes (abiotic, heterotrophic, chemolithoautotrophic) in model simulations can reveal the underlying controls on the distribution and release of CO_2 from a flood plain environment, a critical need within research on subsurface carbon fluxes. The biogeochemical processes affecting carbon dynamics at the site were evaluated using a 2-D, non-isothermal, unsaturated–saturated flow and reactive transport model. Different model simulations highlighted the role of abiotic processes as a major contributor to carbon fluxes in up-gradient locations, while microbial respiration and chemolithoautotrophic oxidation of reduced minerals played a major role in controlling soil CO_2 efflux at a down-gradient location (TT-03) close to the flood plain-Colorado River interface.

We also found significant spatial and temporal heterogeneity in subsurface carbon fluxes at the site. For example, locally high CO_2 concentrations were observed at an NRZ location (TT-03) within the site. The flow and reactive transport modeling suggested that these spatially-variable field observations could not be reproduced without incorporating microbial contributions from chemolithoautotrophic processes (e.g., sulfur and iron oxidation). Results further indicated that temporal variations in modeled CO_2 concentrations were strongly related to soil temperature. Therefore, adequate process representation (abiotic and biotic reactive processes; variably saturated, non-isothermal flow; reactive gas phase) was required to match observed CO_2 concentrations at the site. Including or excluding these processes also yielded large differences in predicted carbon fluxes from the site. Groundwater exports of organic carbon decreased by only 12 % when biotic pathways were included in the simulations; however, atmospheric CO_2 fluxes showed a difference of up to 230 % when these chemolithoautotrophic pathways were included. Results indicated lower overall carbon exports in groundwater when annual water table fluctuations were considered and almost a three-fold increase when annual temperature gradient variations were considered compared to steady water table and temperature simulations. Overall the simulated subsurface carbon exports (DIC flux of 3.3 and DOC flux of 0.3 g m^{-2} d^{-1}) from the site to the river were well within the ranges reported for other flood plain sites (Robertson et al. 1999; Richey et al. 2002; Aufdenkampe et al. 2011). In comparison, the annual atmospheric CO_2 fluxes from the site (8.2 kg m^{-2} d^{-1}) estimated with the model were three orders of magnitude greater than subsurface carbon exports to the river.

Appendix 1

See Tables 10, 11 and Fig. A1.

Table 10 Aqueous complexes considered in the simulations

Reaction	log K (25 °C)	Source
$AlO^+ \leftrightarrow Al^{+3} + H_2O - 2H^+$	10.342	1
$AlO_2^- \leftrightarrow Al^{+3} + 2H_2O - 4H^+$	22.204	1
$AlOH^{+2} \leftrightarrow Al^{+3} + H_2O - H^+$	5.0004	1
$HAlO_2(aq) \leftrightarrow Al^{+3} + H_2O - 3H^+$	15.602	1
$AlSO_4^+ \leftrightarrow Al^{+3} + SO_4^{-2}$	−3.010	1
$Al(Acetate)^{+2} \leftrightarrow Acetate^- + Al^{+3}$	−2.75	3
$Al(Acetate)_2^+ \leftrightarrow 2Acetate^- + Al^{+3}$	−4.600	3

Table 10 continued

Reaction	log K (25 °C)	Source
$CaCl^+ \leftrightarrow Ca^{+2} + Cl^-$	0.293	1
$CaCl_2(aq) \leftrightarrow Ca^{+2} + 2Cl^-$	0.644	1
$CaSO_4(aq) \leftrightarrow Ca^{+2} + SO_4^{-2}$	−2.111	1
$CaOH^+ \leftrightarrow Ca^{+2} + H_2O - H^+$	12.833	1
$CaNO_3^+ \leftrightarrow Ca^{+2} + NO_3^-$	−0.700	1
$CaCO_3(aq) + H^+ \leftrightarrow Ca^{+2} + HCO_3^-$	7.002	1
$CaHCO_3^+ \leftrightarrow Ca^{+2} + HCO_3^-$	−1.047	1
$Ca(Acetate)^+ \leftrightarrow Acetate^- + Ca^{+2}$	−0.930	3
$Ca(Acetate)_2(aq) \leftrightarrow 2Acetate^- + Ca^{+2}$	−1.900	3
$CO_3^{-2} \leftrightarrow HCO_3^- - H^+$	−10.329	1
$CO_2(aq) \leftrightarrow H^+ + HCO_3^- - H_2O$	−6.345	1
$FeO(aq) \leftrightarrow Fe^{+2} + H_2O - 2H^+$	20.405	1
$FeO^+ \leftrightarrow Fe^{+3} + H_2O - 2H^+$	5.650	1
$FeO_2^- \leftrightarrow Fe^{+3} + 2H_2O - 4H^+$	21.620	1
$FeOH^+ \leftrightarrow Fe^{+2} + H_2O - H^+$	9.315	1
$Fe(OH)_3^- \leftrightarrow Fe^{+2} + 3H_2O - 3H^+$	31.000	1
$Fe(OH)_4^{-2} \leftrightarrow Fe^{+2} + 4H_2O - 4H^+$	46.000	1
$FeOH^{+2} \leftrightarrow Fe^{+3} + H_2O - H^+$	2.205	1
$HFeO_2^- \leftrightarrow Fe^{+2} + 2H_2O - 3H^+$	29.207	1
$HFeO_2(aq) \leftrightarrow Fe^{+3} + 2H_2O - 3H^+$	12.018	1
$FeCl^+ \leftrightarrow Fe^{+2} + Cl^-$	0.161	1
$FeCl^{+2} \leftrightarrow Fe^{+3} + Cl^-$	−1.480	1
$FeCl_2(aq) \leftrightarrow Fe^{+2} + 2Cl^-$	8.172	1
$FeS(aq) \leftrightarrow Fe^{+2} + HS^-$	2.200	7
$FeSO_4(aq) \leftrightarrow Fe^{+2} + SO_4^{-2}$	−2.200	1
$FeSO_4^+ \leftrightarrow Fe^{+3} + SO_4^{-2}$	−1.928	1
$FeNO_2^{+2} \leftrightarrow Fe^{+3} + NO_2^-$	−3.150	1
$FeNO_3^{+2} \leftrightarrow Fe^{+3} + NO_3^-$	−1.000	1
$Fe(CO_3)_2^{-2} \leftrightarrow Fe^{+2} + 2HCO_3^- - 2H^+$	−13.498	1
$FeCO_3(aq) \leftrightarrow Fe^{+2} + HCO_3^- - H^+$	4.879	1
$FeHCO_3^+ \leftrightarrow Fe^{+2} + HCO_3^-$	−1.470	1
$Fe(Acetate)^+ \leftrightarrow Acetate^- + Fe^{+2}$	−1.290	3
$Fe(Acetate)_2 \leftrightarrow 2Acetate^- + Fe^{+2}$	−2.485	3
$H(Acetate)(aq) \leftrightarrow Acetate^- + H^+$	−4.76	3
$KOH(aq) \leftrightarrow K^+ + H_2O - H^+$	14.437	1
$KCl(aq) \leftrightarrow K^+ + Cl^-$	2.536	1
$KSO_4^- \leftrightarrow K^+ + SO_4^{-2}$	−0.880	1
$KHSO_4(aq) \leftrightarrow K^+ + SO_4^{-2} + H^+$	1.495	1
$K(Acetate)(aq) \leftrightarrow Acetate^- + K^+$	0.260	3
$MgOH^+ \leftrightarrow Mg^{+2} + H_2O - H^+$	11.683	1
$Mg_4(OH)_4^{+4} \leftrightarrow 4Mg^{+2} + 4H_2O - 4H^+$	39.750	1
$MgCl^+ \leftrightarrow Mg^{+2} + Cl^-$	0.135	1

Table 10 continued

Reaction	log K (25 °C)	Source
$MgSO_4(aq) \leftrightarrow Mg^{+2} + SO_4^{-2}$	−2.300	1
$Mg(Acetate)^+ \leftrightarrow Acetate^- + Mg^{+2}$	−1.280	3
$MgCO_3(aq) + H^+ \leftrightarrow Mg^{+2} + HCO_3^-$	7.350	1
$MgHCO_3^+ \leftrightarrow Mg^{+2} + HCO_3^-$	−1.036	1
$NH_4SO_4^- \leftrightarrow NH_3(aq) + SO_4^{-2} + H^+$	−0.940	1
$HNO_2(aq) \leftrightarrow H^+ + NO_2^-$	−3.225	1
$HNO_3(aq) \leftrightarrow H^+ + NO_3^-$	1.303	1
$NH_4^+ \leftrightarrow H^+ + NH_3(aq)$	−9.241	1
$NaOH(aq) \leftrightarrow Na^+ + H_2O - H^+$	14.205	1
$NaCl(aq) \leftrightarrow Na^+ + Cl^-$	0.777	1
$NaSO_4^- \leftrightarrow Na^+ + SO_4^{-2}$	−0.700	1
$NaCO_3^- + H+ \leftrightarrow Na^+ + HCO_3^-$	9.815	1
$NaHCO_3(aq) \leftrightarrow Na^+ + HCO_3^-$	−0.154	1
$Na(Acetate)(aq) \leftrightarrow Acetate^- + Na^+$	0.100	3
$OH^- \leftrightarrow H_2O - H^+$	13.995	1
$S^{-2} \leftrightarrow HS^- - H^+$	12.935	1
$H_2S(aq) \leftrightarrow H^+ + HS^-$	−6.988	1
$HSO_4^- \leftrightarrow H^+ + SO_4^{-2}$	−1.979	1
$H_2SO_4(aq) \leftrightarrow 2H^+ + SO_4^{-2}$	1.021	1
$HSiO_3^- \leftrightarrow SiO_2(aq) + H_2O - H^+$	9.585	1
$CaHSiO_3^+ \leftrightarrow Ca^{+2} + SiO_2(aq) + H_2O - H^+$	8.575	1
$MgHSiO_3^+ \leftrightarrow Mg^{+2} + SiO_2(aq) + H_2O - H^+$	8.325	1
$NaHSiO_3(aq) \leftrightarrow Na^+ + SiO_2(aq) + H_2O - H^+$	7.754	1

[1] SNL (2007), mostly from Shock et al. (1997)
[2] Rickard (2006)
[3] Reed and Palandri (2006), mostly from Shock and Koretsky (1993) and (Shock et al. 1997)

Table 11 Mineral dissolution/precipitation reactions considered in the simulations

Reaction	log K (25 °C)	Source
$Calcite \leftrightarrow Ca^{+2} + H_2O + HCO_3^- - H^+$	1.849	1
$Goethite \leftrightarrow Fe^{+3} + 2H_2O - 3H^+$	0.176	2
$Siderite \leftrightarrow Fe^{+2} + HCO_3^- - H^+$	−0.192	1
$Pyrite \leftrightarrow Fe^{+2} + 1.75HS^- + 0.25H^+ + 0.25SO_4^{-2} - H_2O$	−24.653	1
$C_6H_{10}O_{5(cellulose)} \leftrightarrow 3Acetate^- + 3H^+ - H_2O$	−34.647	3

[1] SNL (2007), from Shock et al. (1997) and Helgeson et al. (1978)

[2] Adjusted from SNL (2007) for consistency with Majzlan et al. (2004)

[3] Calculated to yield observed background acetate concentrations at the measured field pH near 7
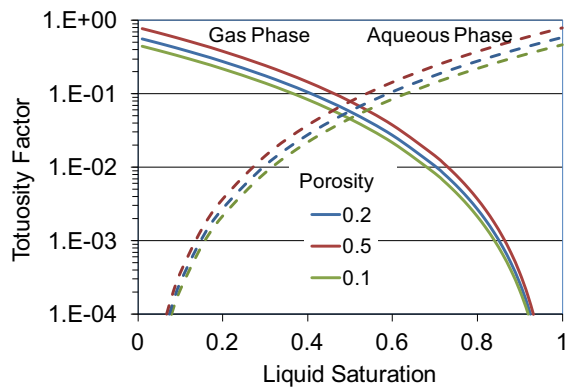
Fig. A1 The tortuosity factor τ is computed as a function of liquid saturation (S_l) and porosity (ϕ) as $\tau_l = S_l^{10/3} \phi^{1/3}$ and $\tau_g = (1 - S_l)^{10/3} \phi^{1/3}$ (Millington and Quirk 1961)

References

Ahonen L, Tuovinen OH (1990) Kinetics of sulfur oxidation at suboptimal temperatures. Appl Environ Microbiol 56:560–562

Amos RT, Mayer KU, Blowes DW, Ptacek CJ (2004) Reactive transport modeling of column experiments for the remediation of acid mine drainage. Environ Sci Technol 38:3131–3138. doi:10.1021/es0349608

Anderson RT, Vrionis HA, Ortiz-Bernad I et al (2003) Stimulating the in situ activity of Geobacter species to remove uranium from the groundwater of a uranium-contaminated aquifer. Appl Environ Microbiol 69:5884–5891

Andrews DM, Lin H, Zhu Q et al (2011) Hot spots and hot moments of dissolved organic carbon export and soil organic carbon storage in the Shale Hills Catchment. Vadose Zo J 10:943. doi:10.2136/vzj2010.0149

Arndt S, Jørgensen BB, LaRowe DE et al (2013) Quantifying the degradation of organic matter in marine sediments: a review and synthesis. Earth-Sci Rev 123:53–86. doi:10.1016/j.earscirev.2013.02.008

Arora B, Mohanty BP, McGuire JT, Cozzarelli IM (2013) Temporal dynamics of biogeochemical processes at the Norman Landfill site. Water Resour Res 49:6909–6926. doi:10.1002/wrcr.20484

Arora B, Dwivedi D, Hubbard SS et al (2015a) Identifying geochemical hot moments and their controls on a contaminated river floodplain system using wavelet and entropy approaches. Environ Model Softw (in press)

Arora B, Şengör SS, Steefel CI (2015b) A reactive transport benchmark on heavy metal cycling in lake sediments. Comput Geosci 19:613–633. doi:10.1007/s10596-014-9445-8

Atkins ML, Santos IR, Ruiz-Halpern S, Maher DT (2013) Carbon dioxide dynamics driven by groundwater discharge in a coastal floodplain creek. J Hydrol 493:30–42. doi:10.1016/j.jhydrol.2013.04.008

Aufdenkampe AK, Mayorga E, Raymond PA et al (2011) Riverine coupling of biogeochemical cycles between land,

oceans, and atmosphere. Front Ecol Environ 9:53–60. doi:10.1890/100014

Bao C, Wu H, Li L et al (2014) Uranium bioreduction rates across scales: biogeochemical "hot moments" and "hot spots" during a biostimulation Experiment at Rifle, Colorado. Environ Sci Technol. doi:10.1021/es501060d

Bargar JR, Campbell KM, Stubbs JE, et al (2011) Speciation and dynamics of biologically reduced uranium(IV) in the Old Rifle aquifer. Abstr Pap Am Chem Soc 242

Batson J, Noe GB, Hupp CR et al (2015) Soil greenhouse gas emissions and carbon budgeting in a short-hydroperiod floodplain wetland. J Geophys Res Biogeosci 120:77–95. doi:10.1002/2014JG002817.Received

Billings SA, Richter DD, Yarie J (1998) Soil carbon dioxide fluxes and profile concentrations in two boreal forests. Can J For Res Can Rech For 28:1773–1783. doi:10.1139/cjfr-28-12-1773

Blazejewski GA, Stolt MH, Gold AJ et al (2009) Spatial distribution of carbon in the subsurface of riparian zones. Soil Sci Soc Am J 73:1733. doi:10.2136/sssaj2007.0386

Bosatta E, Ågren GI (1995) The power and reactive continuum models as particular cases of the q-theory of organic matter dynamics. Geochim Cosmochim Acta 59:3833–3835

Bourg ACM, Bertin C (1993) Biogeochemical processes during the infiltration of river water into an alluvial aquifer. Environ Sci Technol 27:661–666. doi:10.1021/es00041a009

Brunke M, Gonser T (1997) The ecological significance of exchange processes between rivers and groundwater. Freshw Biol 37:1–33. doi:10.1046/j.1365-2427.1997.00143.x

Campbell KM, Kukkadapu RK, Qafoku NP et al (2012) Geochemical, mineralogical and microbiological characteristics of sediment from a naturally reduced zone in a uranium-contaminated aquifer. Appl Geochem 27:1499–1511. doi:10.1016/j.apgeochem.2012.04.013

Cole JJ, Caraco NF (2001) Carbon in catchments : connecting terrestrial carbon losses with aquatic metabolism. Mar Freshw Res 52:101–110

Cole JJ, Prairie YT, Caraco NF et al (2007) Plumbing the global carbon cycle: integrating inland waters into the terrestrial carbon budget. Ecosystems 10:172–185. doi:10.1007/s10021-006-9013-8

Crow SE, Wieder RK (2005) Sources of CO2 emission from a northern peatland: root respiration, exudation, and decomposition. Ecology 86:1825–1834. doi:10.1890/04-1575

Dai Z, Trettin CC, Li C et al (2012) Effect of assessment scale on spatial and temporal variations in CH4, CO2, and N2O fluxes in a forested wetland. Water Air Soil Pollut 223:253–265. doi:10.1007/s11270-011-0855-0

Davidson EA, Samanta S, Caramori SS, Savage K (2012) The dual arrhenius and michaelis-menten kinetics model for decomposition of soil organic matter at hourly to seasonal time scales. Glob Chang Biol 18:371–384. doi:10.1111/j.1365-2486.2011.02546.x

Dermody O, Weltzin JF, Engel EC et al (2007) How do elevated [CO2], warming, and reduced precipitation interact to affect soil moisture and LAI in an old field ecosystem? Plant Soil 301:255–266. doi:10.1007/s11104-007-9443-x

Dick JJ, Tetzlaff D, Birkel C, Soulsby C (2014) Modelling landscape controls on dissolved organic carbon sources and fluxes to streams. Biogeochemistry 122:361–374. doi:10.1007/s10533-014-0046-3

Doussan C, Poitevin G, Ledoux E, Delay M (1997) River bank filtration: modelling of the changes in water chemistry with emphasis on nitrogen species. J Contam Hydrol 25:129–156. doi:10.1016/S0169-7722(96)00024-1

Druhan JL, Bill M, Lim H et al (2014a) A large column analog experiment of stable isotope variations during reactive transport: II. Carbon mass balance, microbial community structure and predation. Geochim Cosmochim Acta 124:394–409. doi:10.1016/j.gca.2013.08.036

Druhan JL, Steefel CI, Conrad ME, DePaolo DJ (2014b) A large column analog experiment of stable isotope variations during reactive transport: i. A comprehensive model of sulfur cycling and δ34S fractionation. Geochim Cosmochim Acta 124:366–393. doi:10.1016/j.gca.2013.08.037

Duckworth OW, Martin ST (2004) Role of molecular oxygen in the dissolution of siderite and rhodochrosite. Geochim Cosmochim Acta 68:607–621. doi:10.1016/S0016-7037(00)00464-2

Eliasson PE, McMurtrie RE, Pepper DA et al (2005) The response of heterotrophic CO2 flux to soil warming. Glob Chang Biol 11:167–181. doi:10.1111/j.1365-2486.2004.00878.x

Etiope G (1999) Subsoil CO 2 and CH 4 and their advective transfer from faulted grassland to the atmosphere. J Geophys Res 104:16889. doi:10.1029/1999JD900299

Fan Z, Neff JC, Waldrop MP et al (2014) Transport of oxygen in soil pore-water systems: implications for modeling emissions of carbon dioxide and methane from peatlands. Biogeochemistry 121:455–470. doi:10.1007/s10533-014-0012-0

Fang Y, Yabusaki SB, Morrison SJ et al (2009) Multicomponent reactive transport modeling of uranium bioremediation field experiments. Geochim Cosmochim Acta 73:6029–6051. doi:10.1016/j.gca.2009.07.019

Farouki OT (1982) Thermal properties of soils. Hanover, New Hampshire

Flores Orozco A, Williams KH, Long PE et al (2011) Using complex resistivity imaging to infer biogeochemical processes associated with bioremediation of an uranium-contaminated aquifer. J Geophys Res 116:G03001. doi:10.1029/2010JG001591

Fox PM, Davis JA, Hay MB et al (2012) Rate-limited U(VI) desorption during a small-scale tracer test in a heterogeneous uranium-contaminated aquifer. Water Resour Res 48:n/a–n/a. doi:10.1029/2011WR011472

Frey SD, Drijber R, Smith H, Melillo J (2008) Microbial biomass, functional capacity, and community structure after 12 years of soil warming. Soil Biol Biochem 40:2904–2907. doi:10.1016/j.soilbio.2008.07.020

Gandy CJ, Smith JWN, Jarvis AP (2007) Attenuation of mining-derived pollutants in the hyporheic zone: a review. Sci Total Environ 373:435–446. doi:10.1016/j.scitotenv.2006.11.004

Handley KM, VerBerkmoes NC, Steefel CI et al (2013) Biostimulation induces syntrophic interactions that impact C, S and N cycling in a sediment microbial community. ISME J 7:800–816. doi:10.1038/ismej.2012.148

Hanson PJ, Edwards NT, Garten CT, Andrews JA (2000) Separating root and soil microbial contributions to soil respiration: a review of methods and observations. Biogeochemistry 48:115–146. doi:10.1023/A:1006244819642

Harshman EN (1972) Geology and uranium deposits, Shirley Basin area. Wyoming, Washington

Helgeson HC, Delany JM, Nesbitt HW, Bird DK (1978) Summary and critique of the thermodynamic properties of rock-forming minerals. Am J Sci 278:229

Helz GR, Adelson JM (2013) Trace element profiles in sediments as proxies of dead zone history; rhenium compared to molybdenum. Environ Sci Technol 47:1257–1264. doi:10.1021/es303138d

Hinton MJ, Schiff SL, English MC (1997) The significance of storms for the concentration and export of dissolved organic carbon from two Precambrian Shield catchments. Biogeochemistry 36:67–88. doi:10.1023/A:1005779711821

Hiscock KM, Grischek T (2002) Attenuation of groundwater pollution by bank filtration. J Hydrol 266:139–144. doi:10.1016/S0022-1694(02)00158-0

Hope D, Billett MF, Cresser MS (1994) A review of the export of carbon in river water: fluxes and processes. Environ Pollut 84:301–324. doi:10.1016/0269-7491(94)90142-2

Hunter KS, Wang Y, Van Cappellen P (1998) Kinetic modeling of microbially-driven redox chemistry of subsurface environments: coupling transport, microbial metabolism and geochemistry. J Hydrol 209:53–80. doi:10.1016/S0022-1694(98)00157-7

Jansen B, Kalbitz K, McDowell WH (2014) Dissolved organic matter: linking soils and aquatic systems. Vadose Zo J. doi:10.2136/vzj2014.05.0051

Kalbitz K, Solinger S, Park JH et al (2000) Controls on the dynamics of dissolved organic matter in soils: a review. Soil Sci 165:277–304. doi:10.1097/00010694-200004000-00001

Kang S, Running SW, Kimball JS et al (2014) Effects of spatial and temporal climatic variability on terrestrial carbon and water fluxes in the Pacific Northwest, USA. Environ Model Softw 51:228–239. doi:10.1016/j.envsoft.2013.09.020

Keller CK, Bacon DH (1998) Soil respiration and georespiration distinguished by transport analyses of vadose CO2, 13CO2, and 14CO2. Global Biogeochem Cycles 12:361–372

Kim JH, Guo X, Park HS (2008) Comparison study of the effects of temperature and free ammonia concentration on nitrification and nitrite accumulation. Process Biochem 43:154–160. doi:10.1016/j.procbio.2007.11.005

Kim DG, Vargas R, Bond-Lamberty B, Turetsky MR (2012) Effects of soil rewetting and thawing on soil gas fluxes: a review of current literature and suggestions for future research. Biogeosciences 9:2459–2483. doi:10.5194/bg-9-2459-2012

Kukkadapu RK, Qafoku NP, Arey BW et al (2010) Effect of extent of natural subsurface bioreduction on Fe-mineralogy of subsurface sediments. J Phys 217:012047. doi:10.1088/1742-6596/217/1/012047

Lasaga AC (1998) Kinetic theory in the earth sciences. Princeton University Press, Princeton

Leirós M, Trasar-Cepeda C, Seoane S, Gil-Sotres F (1999) Dependence of mineralization of soil organic matter on temperature and moisture. Soil Biol Biochem 31:327–335. doi:10.1016/S0038-0717(98)00129-1

Li L, Steefel CI, Williams KH et al (2009) Mineral transformation and biomass accumulation associated with uranium bioremediation at Rifle, Colorado. Environ Sci Technol 43:5429–5435. doi:10.1021/es900016v

Li L, Steefel CI, Kowalsky MB et al (2010) Effects of physical and geochemical heterogeneities on mineral transformation and biomass accumulation during biostimulation experiments at Rifle, Colorado. J Contam Hydrol 112:45–63. doi:10.1016/j.jconhyd.2009.10.006

Long P (2009) Rifle integrated field research challenge site, quarterly report, fiscal year 2009, 2nd and 3rd Quarters

Long PE, Williams KH, Davis JA et al (2015) Bicarbonate impact on U(VI) bioreduction in a shallow alluvial aquifer. Geochim Cosmochim Acta 150:106–124. doi:10.1016/j.gca.2014.11.013

Lovley DR, Phillips EJP (1986) Organic matter mineralization with reduction of ferric iron in anaerobic sediments. Appl Environ Microbiol 51:683–689

Luther GW, Findlay AJ, MacDonald DJ et al (2011) Thermodynamics and kinetics of sulfide oxidation by oxygen: a look at inorganically controlled reactions and biologically mediated processes in the environment. Front Microbiol 2:1–9. doi:10.3389/fmicb.2011.00062

Lynch S, Batty L, Byrne P (2014) Environmental risk of metal mining contaminated river bank sediment at redox-transitional zones. Minerals 4:52–73. doi:10.3390/min4010052

Macpherson GL (2009) CO2 distribution in groundwater and the impact of groundwater extraction on the global C cycle. Chem Geol 264:328–336. doi:10.1016/j.chemgeo.2009.03.018

Maggi F, Gu C, Riley WJ et al (2008) A mechanistic treatment of the dominant soil nitrogen cycling processes: model development, testing, and application. J Geophys Res Biogeosci 113:1–13. doi:10.1029/2007JG000578

Majzlan J, Navrotsky A, Schwertmann U (2004) Thermodynamics of iron oxides: part III, Enthalpies of formation and stability of ferrihydrite ($\sim$ Fe(OH)3/4(S04)1/8), and ε-Fe2O3. Geochmica Cosmochim Acta 68:1049–1059

Mayer KU, Frind EO, Blowes DW (2002) Multicomponent reactive transport modeling in variably saturated porous media using a generalized formulation for kinetically controlled reactions. Water Resour Res 38:13–1–13–21. doi: 10.1029/2001WR000862

McClain ME, Boyer EW, Dent CL et al (2003) Biogeochemical hot spots and hot moments at the interface of terrestrial and aquatic ecosystems. Ecosystems 6:301–312

McKenney DJ, Johnson GP, Findlay WI (1984) Effect of temperature on consecutive denitrification reactions in brookston clay and fox sandy loam. Appl Environ Microbiol 47:919–926

Miall AD (2001) Sedimentary basins: evolution, facies, and sediment budget. Sediment Geol 143:185–186

Millington RJ, Quirk JP (1961) Permeability of porous solids. Trans Faraday Soc 57:1200–1207

Morel FMM, Hering JG (1993) Principles and applications of aquatic chemistry. Wiley, New York

Oba Y, Poulson SR (2009) Oxygen isotope fractionation of dissolved oxygen during abiological reduction by aqueous sulfide. Chem Geol 268:226–232. doi:10.1016/j.chemgeo.2009.09.002

Palandri JL, Kharaka YK (2004) A compilation of rate parameters of water-mineral interaction kinetics for application to geochemical modeling. U.S. geological survey open file report 2004–1068, Menlo Park

Palmer K, Drake HL, Horn MA (2010) Association of novel and highly diverse acid-tolerant denitrifiers with N2O fluxes of an acidic fen. Appl Environ Microbiol 76:1125–1134. doi:10.1128/AEM.02256-09

Parkhurst DL, Appelo CAJ (1999) User's guide to PHREEQC (version 2)—a computer program for speciation, batch-reaction, one-dimensional transport, and inverse geochemical calculations. Denver, CO

Parton WJ, Schimel DS, Cole CV, Ojima DS (1987) Analysis of factors controlling soil organic matter levels in Great Plains grasslands. Soil Sci Soc Am J 51:1173–1179. doi:10.2136/sssaj1987.03615995005100050015x

Pruess K, Oldenburg CM, Moridis GJ (1999) TOUGH2 user's guide version 2. Lawrence Berkeley National Laboratory, Berkeley

Pulliam WM (1992) Carbon dioxide and methane exportsfrom a southeastern floodplain swamp. Ecol Monogr 63:29–53

Qafoku NP, Kukkadapu RK, McKinley JP et al (2009) Uranium in framboidal pyrite from a naturally bioreduced alluvial sediment. Environ Sci Technol 43:8528–8534. doi:10.1021/es9017333

Qafoku NP, Gartman BN, Kukkadapu RK et al (2014) Geochemical and mineralogical investigation of uranium in multi-element contaminated, organic-rich subsurface sediment. Appl Geochemistry 42:77–85. doi:10.1016/j.apgeochem.2013.12.001

Raich JW, Potter CS (1995) Global patterns of carbon-dioxide emissions from soils. Global Biogeochem Cycles 9:23–36. doi:10.1029/94gb02723

Raymond PA, Bauer JE, Cole JJ (2000) Atmospheric CO2 evasion, dissolved inorganic carbon production, and net heterotrophy in the York River estuary. Limnol Oceanogr 45:1707–1717. doi:10.4319/lo.2000.45.8.1707

Reed MH, Palandri JL (2006) SOLTHERM.H06, a database of equilibrium constants for minerals and aqueous species. University of Oregon, Eugene

Richards LA (1931) Capillary conduction of liquids through porous mediums. Physics (College Park Md) 1:318. doi:10.1063/1.1745010

Richey JE, Melack JM, Aufdenkampe AK et al (2002) Outgassing from Amazonian rivers and wetlands as a large tropical source of atmospheric CO2. Nature 416:617–620. doi:10.1038/416617a

Rickard D (2006) The solubility of FeS. Geochim Cosmochim Acta 70:5779–5789. doi:10.1016/j.gca.2006.02.029

Riley WJ, Maggi F, Kleber M et al (2014) Long residence times of rapidly decomposable soil organic matter: application of a multi-phase, multi-component, and vertically resolved model (BAMS1) to soil carbon dynamics. Geosci Model Dev 7:1335–1355. doi:10.5194/gmd-7-1335-2014

Robertson AI, Bunn SE, Boon PI, Walker KF (1999) Sources, sinks and transformations of organic carbon in Australian floodplain rivers. Mar Freshw Res 50:813. doi:10.1071/MF99112

Russell EW (1973) Soil conditions and plant growth, 10th edn. Longmans Publishing, London

Schlesinger WH, Andrews JA (2000) Soil respiration and the global carbon cycle. Biogeochemistry 48:7–20

Schmidt MWI, Torn MS, Abiven S et al (2011) Persistence of soil organic matter as an ecosystem property. Nature 478:49–56

Shock EL, Koretsky CM (1993) Metal-organic complexes in geochemical processes: calculation of standard partial molal thermodynamic properties of aqueous acetate complexes at high pressures and temperatures. Geochim Cosmochim Acta 57:4899–4922. doi:10.1016/0016-7037(93)90128-J

Shock EL, Sassani DC, Willis M, Sverjensky DA (1997) Inorganic species in geologic fluids: correlations among standard molal thermodynamic properties of aqueous ions and hydroxide complexes. Geochim Cosmochim Acta 61:907–950. doi:10.1016/S0016-7037(96)00339-0

Simunek J, Suarez D (1993) Modeling of carbon dioxide transport and production in soil. Water Resour Res 29:487–497

Smith KA, Ball T, Conen F et al (2003) Exchange of greenhouse gases between soil and atmosphere: interactions of soil physical factors and biological processes. Eur J Soil Sci 54:779–791. doi:10.1046/j.1365-2389.2003.00567.x

SNL (2007) Qualification of thermodynamic data for geochemical modeling of mineral-water interactions in dilute systems. Las Vegas, Nevada

Sonnenthal E, Spycher N, Xu T et al (2014) TOUGHREACT V3.0-OMP reference manual: a parallel simulation program for non-isothermal multiphase geochemical reactive transport. Lawrence Berkeley National Laboratory, Berkeley

Southwell M, Thoms M (2011) Patterns of nutrient concentrations across multiple floodplain surfaces in a large Dryland River system. Geogr Res 49:431–443. doi:10.1111/j.1745-5871.2011.00699.x

Spirakis CS (1996) The roles of organic matter in the formation of uranium deposits in sedimentary rocks. Ore Geol Rev 11:53–69. doi:10.1016/0169-1368(95)00015-1

Steefel CI (2000) New directions in hydrogeochemical transport modeling: Incorporating multiple kinetic and equilibrium reaction pathways. Comput Methods Water Resour Vols 1 2 Comput Methods Subsurf Flow Transp—Comput Methods, Surf Water Syst Hydrol 331–338

Steefel CI, Brodie EL, Bouskill N et al (2014) The GEWaSC framework: multiscale modeling of coupled biogeochemical, microbiological, and. Goldschmidt Abstracts. Sacramento, CA, p 2373

Stielstra CM, Lohse KA, Chorover J et al (2015) Climatic and landscape influences on soil moisture are primary determinants of soil carbon fluxes in seasonally snow-covered forest ecosystems. Biogeochemistry. doi:10.1007/s10533-015-0078-3

Stumm W, Morgan JJ (eds) (1993) Aquatic chemistry: chemical equilibria and rates in natural waters. Wiley, New York

Suchomel KH, Kreamer DK, Long A (1990) Production and transport of carbon dioxide in a contaminated vadose zone: a stable and radioactive carbon isotope study. Environ Sci Technol 24:1824–1831. doi:10.1021/es00082a006

Thamdrup B, Hansen JW, Jorgensen BB (1998) Temperature dependence of aerobic respiration in a coastal sediment. FEMS Microbiol Ecol 25:189–200. doi:10.1111/j.1574-6941.1998.tb00472.x

Thornton SF, McManus J (1994) Application of organic carbon and nitrogen stable isotope and C/N ratios as source indicators of organic matter provenance in estuarine systems: evidence from the Tay Estuary, Scotland. Estuar Coast Shelf Sci 38:219–233

Tockner K, Pennetzdorfer D, Reiner N et al (1999) Hydrological connectivity, and the exchange of organic matter and nutrients in a dynamic river-floodplain system (Danube, Austria). Freshw Biol 41:521–535. doi:10.1046/j.1365-2427.1999.00399.x

Tokunaga T, Kim Y, Williams KH et al (2015) Vadose zone borehole instrumentation for monitoring water, solute, and gas fluxes: installations in a cobbly floodplain and initial results. Vadose Zo J 8:1–16

Tufenkji N, Ryan JN, Elimelech M (2002) Peer reviewed: the promise of bank filtration. Environ Sci Technol 36:422A–428A. doi:10.1021/es022441j

U.S. Department of Energy (1999) Final Site Observational Work Plan for the UMTRA Project Old Rifle Site. Grand Junction, CO

U.S. Department of Energy (2012) groundwater compliance action plan for the Old Rifle, Colorado, UMTRCA Title I Processing Site

Van Breukelen BM, Griffioen J, Röling WFM, Van Verseveld HW (2004) Reactive transport modelling of biogeochemical processes and carbon isotope geochemistry inside a landfill leachate plume. J Contam Hydrol 70:249–269. doi:10.1016/j.jconhyd.2003.09.003

Van Cappellen P, Gaillard J-F (1996) Biogeochemical dynamics in aquatic sediments. In: Lichtner PC, Steefel CI, Oelkers EH (eds) Reactive transport in porous media, vol 34. Mineralogical Society of America, Washington, pp 335–376

van Griethuysen C, Luitwieler M, Joziasse J, Koelmans AA (2005) Temporal variation of trace metal geochemistry in floodplain lake sediment subject to dynamic hydrological conditions. Environ Pollut 137:281–294. doi:10.1016/j.envpol.2005.01.023

Vrionis HA, Anderson RT, Ortiz-Bernad I et al (2005) Microbiological and geochemical heterogeneity in an in situ uranium bioremediation field site. Appl Environ Microbiol 71:6308–6318. doi:10.1128/AEM.71.10.6308-6318.2005

Wainwright HM, Orozco AF, Bücker M et al (2015) Hierarchical Bayesian method for mapping biogeochemical hot spots using induced polarization imaging. Water Resour Res n/a–n/a. doi:10.1002/2015WR017763

Waldrop M, Balser T, Firestone M (2000) Linking microbial community composition to function in a tropical soil. Soil Biol Biochem 32:1837–1846. doi:10.1016/S0038-0717(00)00157-7

Walvoord MA., Striegl RG, Prudic DE, Stonestrom DA (2005) CO$_2$ dynamics in the Amargosa Desert: fluxes and isotopic speciation in a deep unsaturated zone. Water Resour Res 41:n/a–n/a. doi: 10.1029/2004WR003599

Wang JH, Baltzis BC, Lewandowski GA (1995) Fundamental denitrification kinetic studies with Pseudomonas denitrificans. Biotechnol Bioeng 47:26–41. doi:10.1002/bit.260470105

Westerhoff P (2003) Reduction of nitrate, bromate, and chlorate by zero valent iron. J Environ Eng 129:10–16. doi:10.1061/(ASCE)0733-9372(2003)129:1(10)

Widdowson MA, Molz FJ, Benefield LD (1988) A numerical transport model for oxygen- and nitrate-based respiration linked to substrate and nutrient availability in porous media. Water Resour Res 24:1553–1565. doi:10.1029/WR024i009p01553

Wilhelm SW, LeCleir GR, Bullerjahn GS et al (2014) Seasonal changes in microbial community structure and activity imply winter production is linked to summer hypoxia in a large lake. FEMS Microbiol Ecol 87:475–485. doi:10.1111/1574-6941.12238

Williams KH, Long PE, Davis JA et al (2011) Acetate availability and its influence on sustainable bioremediation of uranium-contaminated groundwater. Geomicrobiol J 28:519–539. doi:10.1080/01490451.2010.520074

Williamson MA, Rimstidt JD (1994) The kinetics and electrochemical rate-determining step of aqueous pyrite oxidation. Geochim Cosmochim Acta 58:5443–5454

Wójcicki KJ (2012) Stratigraphy of organic-rich deposits in floodplain environments: examples from the upper Odra River basin. Quaest Geogr 31:107–117

Wójcicki KJ, Marynowski L (2012) The organic and mineral matter contents in deposits infilling floodplain basins: holocene alluviation record from the Kłodnica and Osobłoga river valleys, southern Poland. Geomorphology 159–160:15–29. doi:10.1016/j.geomorph.2012.02.020

Wood WW, Petraitis MJ (1984) Origin and distribution of carbon dioxide in the unsaturated zone of the southern high plains of texas. Water Resour Res 20:1193–1208. doi:10.1029/WR020i009p01193

Wu Y, Ajo-Franklin JB, Spycher N et al (2011) Geophysical monitoring and reactive transport modeling of ureolytically-driven calcium carbonate precipitation. Geochem Trans 12:7. doi:10.1186/1467-4866-12-7

Xu T, Spycher N, Sonnenthal E et al (2011) TOUGHREACT Version 2.0: a simulator for subsurface reactive transport under non-isothermal multiphase flow conditions. Comput Geosci 37:763–774. doi:10.1016/j.cageo.2010.10.007

Yabusaki SB, Fang Y, Williams KH et al (2011) Variably saturated flow and multicomponent biogeochemical reactive transport modeling of a uranium bioremediation field experiment. J Contam Hydrol 126:271–290. doi:10.1016/j.jconhyd.2011.09.002

Zogg GP, Zak DR, Ringelberg DB et al (1997) Compositional and functional shifts in microbial communities due to soil warming. Soil Sci Soc Am J 61:475. doi:10.2136/sssaj1997.03615995006100020015x